

2026 Chapter 4

2027 Ross Ice Shelf bathymetry inversion

2028 Abstract

2029 Antarctica's Ross Ice Shelf buttresses a large catchment of ice from both the East
2030 and West Antarctic Ice Sheets. Changes to the current steady state of the ice
2031 shelf, likely through basal melt of the sensitive grounding zones, will reduce this
2032 buttressing and accelerate the Antarctic Ice Sheet's contribution to global sea level
2033 rise. The distribution of basal melt is predominantly controlled by the ocean cavity
2034 thickness and the channelling of ocean waters by bathymetric features. Here we
2035 use airborne gravity data and distributed seismic constraints across the ice shelf
2036 to create an updated sub-ice shelf bathymetry model. We accomplish this with a
2037 non-linear geometric gravity inversion, available as open-source Python code. Monte
2038 Carlo sampling of the inversion inputs provides a robust means of addressing spatial
2039 uncertainty and the relative significance of each component of the inversion. The
2040 resulting bathymetry closely matches the seismic constraints and reveals significant
2041 changes compared to past bathymetry models. We find several likely locations of
2042 past pinning points, locations where enhanced basal melting is likely, and sites of
2043 possible tectonic significance.

2044 Key Points

- 2045 1. We present a new bathymetry model beneath Antarctica's Ross Ice Shelf from
2046 a gravity inversion
- 2047 2. A Monte Carlo simulation provides a detailed spatial uncertainty analysis
- 2048 3. Results highlight locations where basal melting may be enhanced or where the
2049 shelf may have been recently grounded

2050 4.1 Introduction

2051 Much of Antarctica's coastline is fringed by floating extensions of the Antarctic Ice
2052 Sheet. These floating masses of ice, referred to as ice shelves, are connected to the
2053 grounded ice. Over 80% of Antarctica's grounded ice drains to the oceans through
2054 these ice shelves (Dupont & Alley, 2005). While they are floating, and thus already
2055 displace their mass equivalent of seawater, they are vital to the future contribution
2056 of the Antarctic Ice Sheet to global sea level rise (Fürst et al., 2016; Jacobs et al.,
2057 1992). The ice shelves slow the flow of upstream ice into the ocean by imparting

Not definitive
reference for
two
(current and
future)

a resistive force, known as buttressing. This buttressing occurs from lateral drag along the sides of the ice shelves and resistive stresses incurred where they flow over pinning points (localized areas of grounded ice) (Dupont & Alley, 2005; Matsuoka et al., 2015). Changes to the geometry of the ice shelves can reduce their restraining effect on the flow of grounded ice, leading to an increased mass flux of ice across the grounding zone, thus increasing the ice sheet's contribution to global sea level rise (e.g., Pritchard et al., 2012; Scambos et al., 2004).

2065

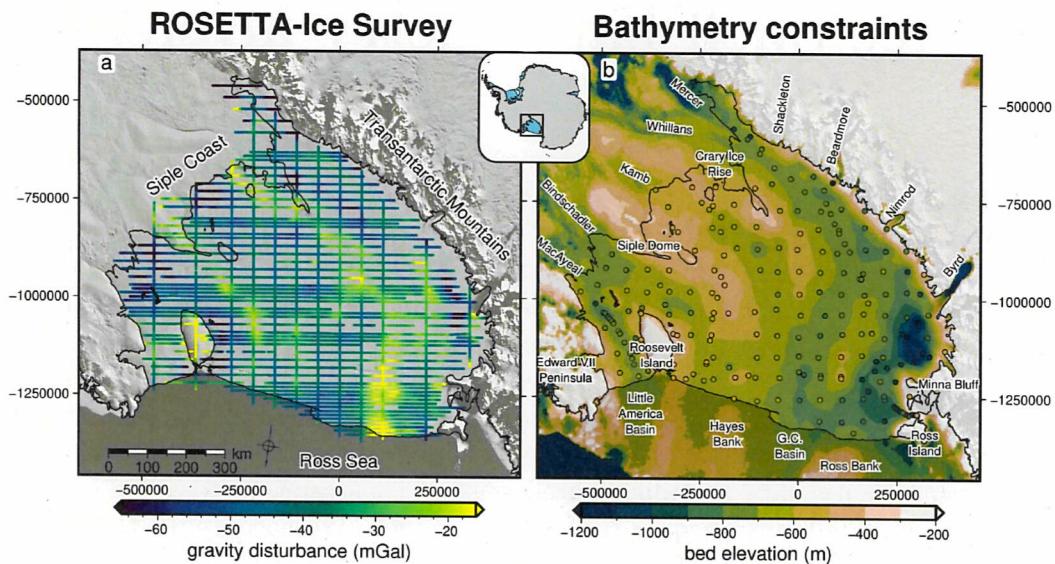


Figure 4.1: Input datasets for the Ross Ice Shelf bathymetry inversion. **a)** ROSETTA-Ice airborne gravity disturbance data (cleaned and re-leveled). **b)** Bedmap2 bed elevations in background, with individual constraint points within the ice shelf boundary (dots) on the same color scale. Black line in both figures shows the grounding line and ice front from Mouginot et al. (2017). Background imagery is from MODIS-MOA (Scambos et al., 2007). Regional names shown in **a** and specific location names shown in **b**, which include ice streams along the Siple Coast, outlet glaciers along the Transantarctic Mountains, and bathymetry features in the Ross Sea. The RMS difference between the constraint point values and the BedMap2 gridded values is 138 m.

The largest ice shelf is the Ross Ice Shelf (Figure 4.1, Fretwell et al., 2013). Situated between East and West Antarctica, the Ross Ice Shelf comprises ice from both the East and West Antarctic Ice Sheets; a catchment with a total of 11.6 meters of potential global sea level rise (Tinto et al., 2019). While the Ross Ice Shelf is in approximate steady-state, that is a near net-zero mass change (e.g., Moholdt et al., 2014; Rignot et al., 2013), geologic evidence shows rapid disintegration (Naish et al., 2009; Yokoyama et al., 2016) and extensive grounding line retreat (Venturelli et al., 2020; Spector et al., 2017) have occurred as recently as the mid-Holocene (~ 7 kyr B.P.). Ocean forcing, specifically basal melting along the grounding zone, is thought to drive these rapid grounding line retreats (Lowry et al., 2019). The current stability of the ice shelf is in part attributed to the lack of warm Circumpolar Deep Water penetrating into the cavity (Tinto et al., 2019; Dinniman et al., 2011). Ocean waters that do penetrate the cavity, such as High Salinity Shelf Water, are dense and relatively cold. Despite their temperature, they are responsible for significant melting at the large depths of the grounding zone (Adusumilli et al., 2020) due to the pressure suppression of the freezing temperature of ice (Tinto et al., 2019).

2082

ambiguous

2083 Thèse waters are formed on the continental shelf from the creation of sea ice.
 2084 Due to their density and the reverse slope of the continental shelf, they flow into
 2085 the cavity, guided by bathymetric troughs (Tinto et al., 2019; Jacobs et al., 1992).
 2086 There are many examples of bathymetric features controlling the routing of these
 2087 sub-shelf waters (e.g., Dutrieux et al., 2014; De Rydt et al., 2014; Zhao et al., 2019;
 2088 Gladish et al., 2015). Additionally, ocean modelling sensitivity testing highlights
 2089 the importance of bathymetric features to sub-shelf circulations and melt (De Rydt
 2090 et al., 2014; Goldberg et al., 2020). From this, bathymetry ~~surface~~ plays a key role in the
 2091 stability of the Ross Ice Shelf through its likely control on the basal melt magni-
 2092 tude and distribution (Goldberg et al., 2019), and through the buttressing effect of
 2093 bathymetric pinning points (Still et al., 2019).

2094

2095 Direct observations of the sea floor beneath the Ross Ice Shelf (excluding along
 2096 its periphery) are limited to two drill holes. The first was the 1977 J9 drill hole north
 2097 of Crary Ice Rise as part of the Ross Ice Shelf Project (Clough & Hansen, 1979). The
 2098 second was the 2017 HWD2 drill hole near the centre of the ice shelf (Stevens et al.,
 2099 2020). Apart from these two drill holes, all other inferences of sub-shelf bathymetry
 2100 depths have been from seismic surveying, or the gravity inversion of Tinto et al.
 2101 (2019). The majority of seismic surveys on the Ross Ice Shelf were accomplished
 2102 during two projects, the International Geophysics Year traverses of the late 1950's
 2103 and early 1960's (Crary, 1959; Crary et al., 1962; Crary & Robinson, 1962), and the
 2104 Ross Ice Shelf Geophysical and Glaciological Survey (RIGGS, 1973-1974 Bentley,
 2105 1984). These extensive surveys systematically covered the entire ice shelf, collecting
 2106 223 observations of bathymetry with a mean spacing of approximately 40 km be-
 2107 tween points (Figure 4.1b).

2108

or 55 km?

ambiguous

2109 These data have been included in various Antarctic bed / bathymetry products
 2110 (Fretwell et al., 2013; Le Brocq et al., 2010; Timmermann et al., 2010). As discussed
 2111 later, Tinto et al. (2019) conducted a gravity inversion over the entirety of the ice
 2112 shelf with data from the Ross Ocean and ice Shelf Environment, and Tectonic set-
 2113 ting Through Aerogeophysical surveys and modelling project (ROSETTA-Ice). This
 2114 provided a significantly improved resolution over just the interpolation of the sparse
 2115 seismic data. This gravity-inverted bathymetry was later incorporated in the Bed-
 2116 Machine bed compilation (Morlighem et al., 2020; Morlighem, 2022). This chapter
 2117 focuses on once again improving the sub-Ross Ice Shelf Bathymetry model. Follow-
 2118 ing Tinto et al. (2019), we also use a gravity inversion of the ROSETTA-ice data to
 2119 model the bathymetry. However, we conduct additional and careful processing of
 2120 the gravity data, and apply it to an entirely new gravity inversion algorithm, as de-
 2121 scribed in Chapter 3. Additionally, our method provides an assessment of the spatial
 2122 uncertainty of the resulting model, a vital component needed for the ocean mod-
 2123 elling community to know where to focus efforts (Goldberg et al., 2020). [The basis
 2124 of modelling bathymetry with a gravity inversion is that the bathymetry surface,
 2125 which is a contrast between lower-density material (seawater) and higher-density
 2126 material (sediment) creates a measurable effect on Earth's gravity.]

2127

{Belong here?}

2128 4.2 Methods

2129 Here we describe the three main methodologies of this chapter; 1) the gravity reduction
 2130 process, from observed data to the topo-free gravity disturbances (Figure 4.2a),
 2131 2) the bathymetric inversion process (Figure 4.2b), which is explained in detail in
 2132 Chapter 3 and briefly re-introduced here, and 3) the use of a Monte Carlo simulation
 2133 to quantify spatial uncertainty in the resulting bathymetry (Figure 4.7).

*Not useful
as not yet
defined.*
*Figs
should
be
referenced
in order*

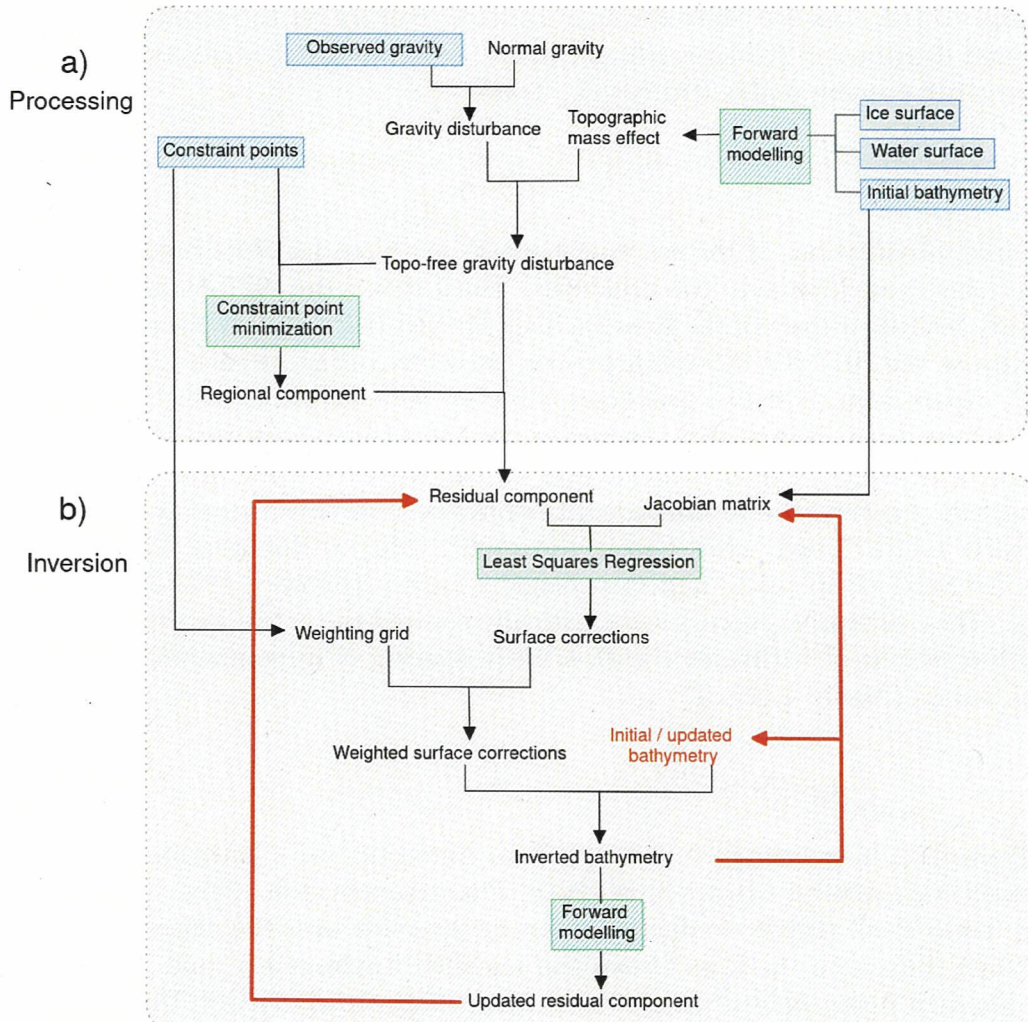


Figure 4.2: Schematic workflow diagram for a) gravity processing steps and b) running the inversion. Blue boxes show the input datasets, green boxes show the key processes and red lines signify iterative components of the inversion.

2134 4.2.1 Gravity reduction

2135 A common task in geophysics is the removal of predictable noise to help amplify the
 2136 signal of interest. This is the basis of gravity reduction; the process of isolating the
 2137 desired gravity signal from the raw measurements of the Earth's gravitational field.
 2138 The magnitude of Earth's gravitational acceleration, which we will refer to as *gravity*,
 2139 ranges from $\sim 978,000$ to $\sim 983,000$ mGal, from the equator to the
 2140 poles, respectively (Hofmann-Wellenhof & Moritz, 2006). The range in these values,

2141 approximately 5000 mGal, vastly outweighs the typical values of gravity anomalies
 2142 resulting from geologic features of interest. These anomalies of interest are typically
 2143 on the order of magnitude of 10's of mGal. This exemplifies the issue of removing
 2144 *noise* which has a significantly greater magnitude than the *signal* of interest.

2145
 2146 Here, we start the gravity reduction process with observed gravity. We take ob-
 2147 served gravity to be the signal which is produced by 1) the gravitational attraction
 2148 of all massive bodies in Earth and 2) the rotation of the Earth. This means non-
 2149 geological and time-dependent effects such as machine drift, tidal changes, aircraft
 2150 manoeuvres and the effect of measuring gravity on a moving platform (Eötvös cor-
 2151 rection) have already been removed from the observed gravity (Hinze et al., 2005;
 2152 Hinze et al., 2013). With this, observed gravity is defined as;

$$g_{obs}(p) = \gamma(p) + g_{geology}(p) \quad (4.1)$$

2153 where, for an observation point p , $g_{obs}(p)$ is the observed gravity, $\gamma(p)$ is the
 2154 attraction of the *normal* Earth and $g_{geology}(p)$ encompasses the gravity effects of all
 2155 deviations between the *normal* Earth and the real Earth. This *normal* Earth is
 2156 often taken as a single surface (here the reference ellipsoid) with a constant density
 2157 above (ρ_{air}) and a constant density below (ρ_{crust}). Therefore, deviations between
 2158 the *normal* and real Earth include 1) any masses above the ellipsoid which don't
 2159 have the uniform density of air or 2) any masses below the ellipsoid which don't
 2160 have the uniform density of crust. For a bathymetry inversion, the gravity signal of
 2161 interest is a component of $g_{geology}$, which we must isolate from γ . ✓

2162 4.2.1.1 Attraction of normal Earth

2163 Observed gravity varies greatly due to the observation point's position, both based
 2164 on latitude and elevation. Due to the oblate shape of the Earth, gravity is generally
 2165 lower at low latitudes due to 1) increased distance from the center of Earth's mass,
 2166 and 2) more importantly, the increased angular velocity (Jacoby & Smilde, 2009).
 2167 Additionally, there is a decay of gravity with increased elevation, due to an increased
 2168 distance from the center of Earth's mass. These effects aren't related to the geologic
 2169 variations of interest and thus should be removed. Historically, these effects of
 2170 latitude and elevation were approximated separately, using the International Gravity
 2171 Formula (*Latitude correction*) and the *Free-air correction*, respectively (Hinze et al.,
 2172 2005). Alternatively, Li and Götze (2001) derived an analytical solution to the
 2173 gravity effects of an ellipsoid, at any point on or above its surface¹. With this,
 2174 the Latitude and Free-air corrections are combined, and their approximations are
 2175 replaced with closed-form solutions. By subtracting the normal gravity from the
 2176 observed gravity at each observation point the gravity disturbance is found, where

$$\delta g(p) = g_{obs}(p) - \gamma(p), \quad (4.2)$$

2177 where for an observation point p , $\delta g(p)$ is the gravity disturbance, $g_{obs}(p)$ is
 2178 the observed gravity, and $\gamma(p)$ is the normal gravity (*Understanding the Bouguer*

¹Note that the normal gravity calculation with this analytical solution is not valid below the ellipsoid. While this is irrelevant for most locations on Earth, West Antarctic has negative geoid elevations, meaning observations near sea level are likely below the reference ellipsoid, invalidating the normal gravity calculation. For these situations, the use of a quasi-ellipsoid is recommended (Vajda et al., 2008a; *Understanding the Bouguer Anomaly*, 2017)

2179 Anomaly, 2017).

2180

2181 The observation point, p , is defined by three coordinates; latitude, longitude, and
 2182 geometric height (ellipsoidal height). It is a common mistake in geophysical studies
 2183 for the normal gravity calculation to use the point p 's orthometric height (geoidal
 2184 height or mean sea level), instead of its geometric height (Oliveira et al., 2018). This
 2185 results in the calculation of normal gravity at a different point in 3D space relative
 2186 to the observation. This calculation, while truly determining the gravity anomaly
 2187 (a.k.a. free-air anomaly), is not well-suited for geological interests because the grav-
 2188 ity anomaly contains signal from centrifugal acceleration effects due to the different
 2189 locations of the points. Conversely, the gravity disturbance is defined as the differ-
 2190 ence between gravity and normal gravity at the same point, and thus only contains
 2191 signal resulting from geologic sources (Hofmann-Wellenhof & Moritz, 2006). The
 2192 difference between the gravity anomaly and the disturbance for Antarctica ranges
 2193 from -20 to +20 mGal (See Figure C.1 in appendix C for a comparison). It is com-
 2194 mon for studies to correctly use the gravity disturbance while referring to it as the
 2195 free-air anomaly to adhere to tradition. Combining Equations 4.1 and 4.2, shows
 2196 that the gravity disturbance, δg , results solely from deviations between the theo-
 2197 retical model of the Earth (the *normal* Earth) and the true density variations and
 2198 topography of the Earth (Vajda et al., 2004). Figure 4.3 compares observed grav-
 2199 ity, normal gravity, the gravity disturbance, and the gravity anomaly for Antarctica.

2200

2201 4.2.1.2 Topographic mass effects

2202 Typically, geophysical studies are interested in interpreting or inverting gravity sig-
 2203 nals resulting from subsurface features. To accommodate this, all other gravity
 2204 effects must be computed and removed from the gravity disturbance. These other
 2205 effects include the gravity resulting from masses bound by known surfaces, referred
 2206 to as *topographic* or *terrain masses*. These surfaces include, but are not limited to,
 2207 the rock surface (topography), the ocean surface (geoid), the seafloor (bathymetry),
 2208 and the ice surface. Together, the gravity resulting from these masses is referred to
 2209 as the *topographic mass effect*. Correcting the gravity disturbance for these topo-
 2210 graphic masses yields the *topo-free gravity disturbance* δg_{TC} , where

$$\delta g_{TC}(p) = \delta g(p) - g_{topo}(p). \quad (4.3)$$

2211 $g_{topo}(p)$ represents the summed topographic mass effect. δg_{TC} is sometimes re-
 2212 ferred to as the *Bouguer disturbance*, owing to the historic use of the *Bouguer
 2213 anomaly*. In accordance with Vajda et al. (2007), we refer to it as the *topo-free
 2214 gravity disturbance* to clarify that the ellipsoid has been used instead of the geoid
 2215 in all reduction steps. In the past, the topographic mass effect has been split into
 2216 the Bouguer slab correction and the terrain correction. The Bouguer slab correction
 2217 approximates the topographic masses as laterally infinite flat slabs, while the terrain
 2218 correction accounts for the overestimation of the Bouguer slab resulting from the
 2219 assumption of the flat slab. With modern computing able to efficiently calculate the
 2220 gravity resulting directly from a topographic surface (Project et al., 2023), there is
 2221 no need for the separate two-step correction.

2222

Name?

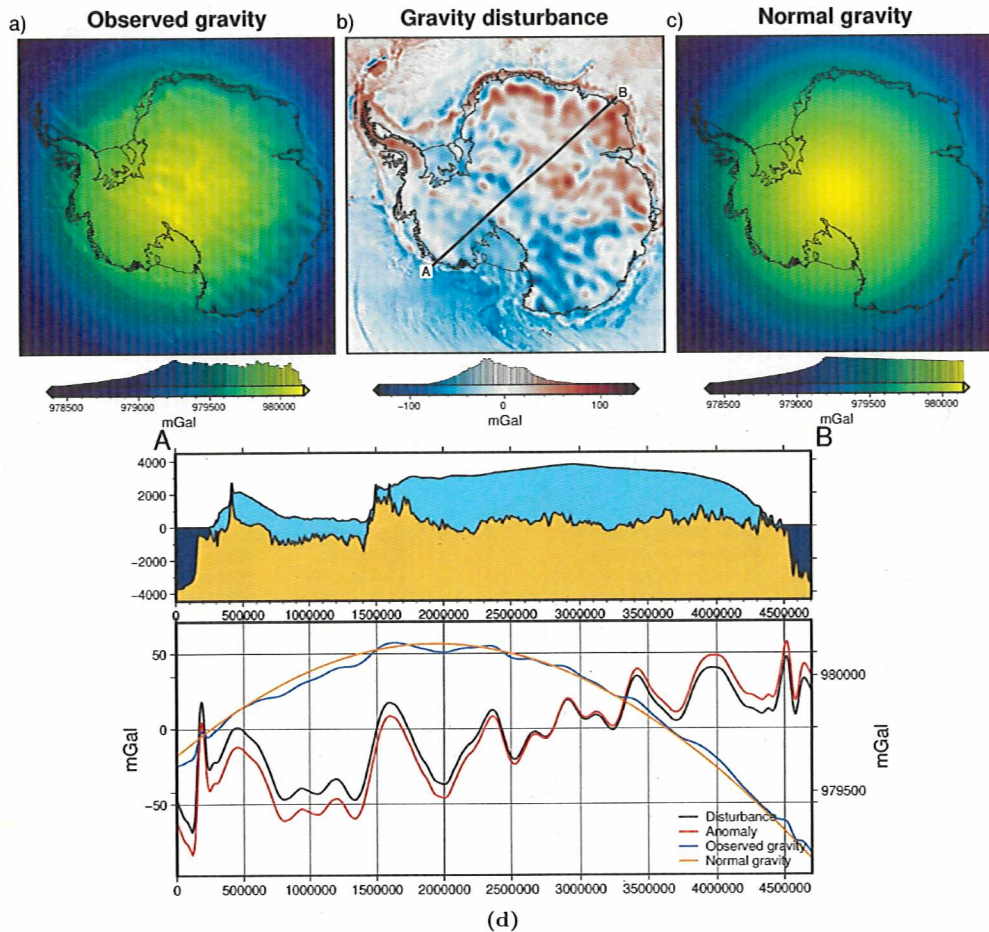


Figure 4.3: Observed gravity data reduction for Antarctica. **a)** Observed gravity data from Förste et al. (2014) at a geodetic observation height of 10 km. **b)** The gravity disturbance at 10 km height, defined as **a-c**. **c)** The normal gravity calculated at the same observation points as **a** using the closed-form equations of Li and Götze (2001). **d)** Profile A-B across Antarctica, location shown in **b**. Gravity disturbance (black) and anomaly (red) values are on the left y-axis, while observed (blue) and normal (orange) gravity values are on the right y-axis.

The topographic mass effect reflects all topographic deviations (including topography of the ice, water, and seafloor) between the *normal* Earth and the real Earth. The *normal* Earth model is shown in Figure 4.4a, as defined by air above the ellipsoid and crust below. A simplified model of the true Earth is shown in Figure 4.4b, and contains air, ice, water, crust, and various geologic bodies within the crust. These masses are separated in Figure 4.4c into components above and below the ellipsoid. From this, the masses which are anomalous with respect to the *normal* Earth can be distinguished, as shown in Figure 4.4d. These anomalous masses include water, ice, and crust above the ellipsoid, and air, ice, water, and geologic bodies below the ellipsoid. The gravitational effect of these anomalous masses can be approximated by assuming each mass's density and setting it relative to the density of the component of the *normal* Earth which the mass is replacing. These relative densities are shown in the key of Figure 4.4d. Calculating and summing the gravity effect of each of the components of Figure 4.4d (excluding the geologic bodies) gives the topographic mass effect. Subtracting this from the gravity disturbance gives the topo-free gravity disturbance².

²The use of the reference ellipsoid as the bounding surface of the topographic mass effect

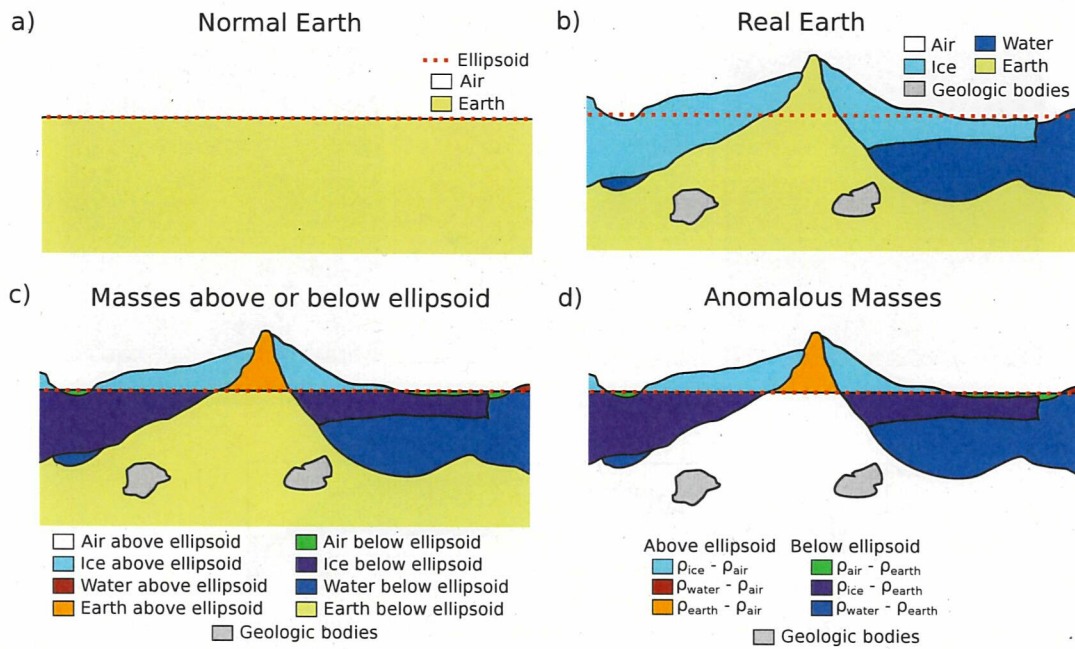


Figure 4.4: Components of the topographic mass effect and resulting topo-free gravity disturbance, or Bouguer disturbance. **a)** The normal Earth model, **b)** a simplified real Earth model. **c)** Topographic masses separated into components above and below the ellipsoid. **d)** Real Earth topographic masses which are anomalous with respect to the normal Earth. Note if the reference level (red dashed line) is switched from the ellipsoid to the geoid, this would result in a Bouguer anomaly.

2239

2240 *are* To compute the topographic mass effect, the anomalous masses from Figure 4.4d
 2241 must be discretized into a series of vertical right-rectangular prisms. To achieve the
 2242 geometry and density configuration of Figure 4.4d, three sets of prisms are used, as
 2243 shown in Figure 4.5c-e.

- 2244 1. Prisms between the ice surface and the ellipsoid are assigned densities of $\rho_{ice} - \rho_{air}$ for prisms above the ellipsoid, and $\rho_{air} - \rho_{ice}$ for prisms below the ellipsoid.
- 2245 2. Prisms between the water surface (ice base) and the ellipsoid are assigned densities of $\rho_{water} - \rho_{ice}$ for prisms above the ellipsoid, and $\rho_{ice} - \rho_{water}$ for prisms below the ellipsoid.
- 2246 3. Prisms between the rock surface (topography onshore and bathymetry offshore)
 2247 and the ellipsoid are assigned densities of $\rho_{rock} - \rho_{water}$ for prisms above
 2248 the ellipsoid, and $\rho_{water} - \rho_{rock}$ for prisms below the ellipsoid.

2249 This configuration of prisms correctly discretizes the topographic mass effect be-
 2250 cause the ice surface is equal to the water surface in areas of no ice thickness, and
 2251 the water surface is equal to the rock surface in areas of no water thickness. Due
 2252 to this, the overlap between the three sets of prisms, shown in Figure 4.5b gives the
 2253 appropriate densities, as defined in Figure 4.4d. From these three sets of prisms, the
 2254 topographic mass effect can be calculated at the gravity observation points using the
 2255 analytical solutions of Nagy et al. (2000). As a demonstration, the topographic mass

2256 calculations results in a topo-free gravity disturbance while using the geoid as the bounding surface
 2257 would result in a Bouguer anomaly (Vajda et al., 2006).

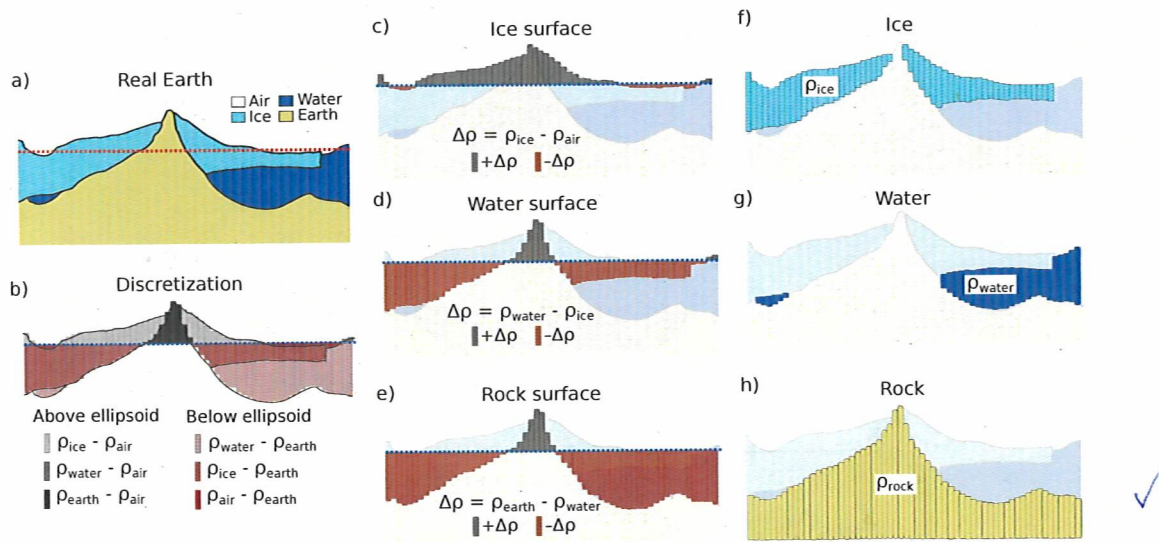


Figure 4.5: Discretizing the topographic mass effect. **a)** The simplified real Earth model, with air, ice, water, and earth. **b)** the resulting anomalous masses relative to the *normal* Earth, as shown in Figure 4.4d. **c)** Prisms between the ellipsoid and the ice surface, **d)** prisms between the ellipsoid and the water surface (ice base), and **e)** prisms between the ellipsoid and the rock surface (topography onshore and bathymetry offshore). Overlap of prisms from **c-e** creates the different shades shown in **b**. The alternative discretization approach, commonly used, is shown in **f-h** where the prism layers are bound both above and below by topographic layers, or arbitrary references (bottom of prisms in **h**), instead of by the normal Earth reference surface (ellipsoid). Additionally, density values of the prisms are related to the material they discretize and are not relative to the expected density of the normal Earth.

justify this choice

2259 effect for Antarctica is calculated using topographic data from Bedmap2 (Fretwell
 2260 et al., 2013), referenced to the WGS-84 ellipsoid. The calculated topographic mass
 2261 effect, the gravity disturbance, the resulting topo-free gravity disturbance, and the
 2262 topographic mass effect from the alternative method of discretization (Figure 4.5f-h)
 2263 are shown in Figure 4.6.

2264

2265 The theoretical topo-free gravity disturbance is the gravity effect caused by and
 2266 only by anomalous subsurface bodies, which have a density different from the as-
 2267 sumed constant density of the crust. In reality, there are additional components of
 2268 the topo-free gravity disturbance resulting from 1) noise in the observed data, 2)
 2269 non-uniform densities used in the topographic mass effect calculation, and 3) inac-
 2270 curate topographic data used for the topographic mass effect calculation. In most
 2271 geophysical applications, the uncertainty of the topographic data is small compared
 2272 to other uncertainties in the analysis, and thus component #3 is assumed to be zero.
 2273 Conversely, for the case of a bathymetry inversion, this component of the topo-free
 2274 disturbance resulting from the inaccuracies of the topography (bathymetry) data is
 2275 the signal of interest. Next, we will isolate this component from the remainder of
 2276 the topo-free gravity disturbance.

2277

2278 4.2.1.3 Regional separation

2279 Here, we separate the topo-free gravity disturbance into components resulting from
 2280 1) subsurface geologic variations and 2) inaccuracies between the true bathymetry
 2281 and the low-resolution bathymetry data used for the terrain mass effect. These

very clear.

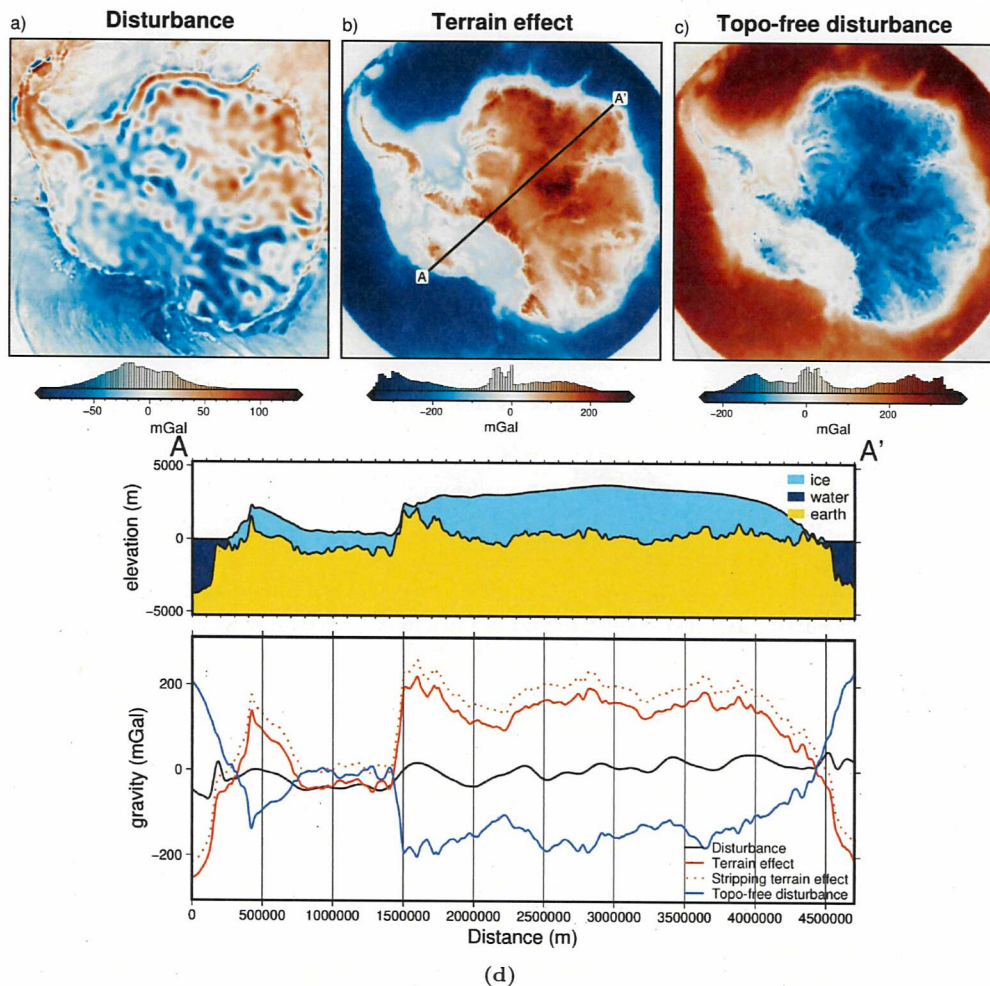


Figure 4.6: Topographic mass effect at 10 km height for Antarctica, from Bedmap2 topographic data (Fretwell et al., 2013). **a)** Gravity disturbance at a geodetic observation height of 10 km, from Figure 4.3b. **b)** The combined gravity effect of the anomalous masses defined in Figure 4.4d and discretized following 4.5b. **c)** The topo-free gravity disturbance, calculated as **a** - **b**. **d)** Profile A-A' across Antarctica, location shown in **b**. The dotted red line shows the terrain mass effect results of the alternative discretization method shown in Figure 4.5f-h. A DC shift was applied to attempt to remove the offset.

are referred to as the regional and residual components, respectively. Chapter 3 highlighted the importance of accurately estimating and separating this regional component from the residual. It was found to be the largest source of uncertainty in several synthetic bathymetry inversions, as well as other Antarctic bathymetry inversions (Brisbourne et al., 2014). While there are many techniques to estimate the regional component, we will use constraint point minimization due to its demonstrated effectiveness over the other methods (Section 3.2.4). This technique samples the topo-free gravity disturbance at points of known bathymetry depth, referred to as the constraint points. Since the depth is known here, the residual component of gravity should be near zero, and thus the regional component should entirely equal the topo-free gravity disturbance. Using these sampled values, the entire model domain is gridded with an interpolation, using either bi-harmonic splines (Uieda, 2018) or minimum curvature (Smith & Wessel, 1990). The resulting grid makes up the regional component, and when subtracted from the topo-free gravity disturbance gives the residual component. This residual component is the input into the

2297 inversion.

2298

2299 4.2.2 Bathymetry inversion

2300 Here we start by briefly summarising the bathymetry inversion workflow described in
2301 Chapter 3, and shown schematically in Figure 4.2b. Then we compare our method to
2302 several other commonly used bathymetry inversion algorithms. Our inversion begins
2303 by computing the Jacobian matrix (Equation 3.8), which is a quantitative means
2304 of describing the sensitivity of the residual gravity data to changes in the height of
2305 each grid cell of bathymetry. In other words, the Jacobian quantifies the ratio be-
2306 between the amplitude of bathymetric features and the gravity anomaly resulting from
2307 them. From this Jacobian matrix, the optimal change to apply to each bathymetry
2308 grid cell to minimize the residual gravity data is estimated. This is in the form of
2309 a surface correction grid, with a value for each grid cell of bathymetry. Since there
2310 are locations of already known bathymetry depths (constraint points), this surface
2311 correction grid should be zero at these points. To achieve this, a weighting grid is
2312 calculated, which is based on the minimum distance between each grid cell and the
2313 nearest constraint point. These distance values are then normalized from 0 to 1,
2314 with 0 being the cells closest to the constraints, and 1 being the cells furthest. The
2315 surface correction grid is multiplied by this weighting grid, to achieve a correction
2316 value of 0 m at the constraints, smoothly tapering off to the full estimated correction
2317 values at a distance.

2318

2319 With this weighted surface correction grid, the original bathymetry depths are
2320 updated. To ensure the updated bathymetry doesn't intersect the ice base, the ice
2321 base topography is set as an upper-bounding surface. The forward gravity of this
2322 updated bathymetry is then re-calculated, with the prism configuration and densi-
2323 ties shown in Figure 4.5e. The updated forward gravity is used to recalculate the
2324 topo-free gravity disturbance. Using the same regional component as calculated be-
2325 fore the inversion (Section 4.2.1.3), an updated residual gravity is computed. This
2326 is then input into the next iteration of the inversion (red lines in Figure 4.2b). Iter-
2327 ations continue until a set of user-defined stopping criteria are met; 1) a maximum
2328 number of iterations is reached, 2) a minimum value of the ℓ^2 -norm of the residual
2329 is reached, or 3) there is no significant variation in the ℓ^2 -norm in two consecutive
2330 iterations.

2331

2332 This process describes a single *inversion*. The critical step in this inversion, deter-
2333 mining the surface correction values from the sensitivity matrix, includes a damping
2334 parameter that controls the smoothness of the resulting inverted bathymetry. This
2335 damping parameter value directly affects the resulting bathymetry model and needs
2336 to be carefully chosen. For this, we follow the cross-validation routine described in
2337 Chapter 3 from Uieda and Barbosa (2017). This involves running the entire inver-
2338 sion for a suite of different damping parameter values. The input gravity data to
2339 these inversions is split into a *testing* set and a *training* set. The inversion only
2340 uses the *training* set. After each inversion, the forward gravity effect of the updated
2341 bathymetry model is calculated at the points of the *testing* set. The root mean
2342 squared difference between the testing gravity values and the forward gravity values
2343 gives the *score* of each cross-validation. The damping parameter which produces



2344 the lowest score is chosen as the optimal value.

2345

2346 4.2.3 Starting bathymetry

2347 An initial bathymetry model for the inversion is needed to compute the topographic
2348 mass effect and to run the inversion. The weighting grid constrains the inversion
2349 from changing the starting grid values at the constraint points. For this reason,
2350 the starting model should be carefully created. As discussed in the previous chapter
2351 (Chapter 3, Section 3.4.2), there are several methods of creating the starting
2352 model from the sparse measurements at the constraint points. Here, we use and
2353 compare two techniques for interpolating these constraint point values over the en-
2354 tire domain; tensioned minimum curvature (Smith & Wessel, 1990) and bi-harmonic
2355 splines (Sandwell, 1987). See Chapter 3 Section 3.4.2 for the details of these gridding
2356 techniques. Figure 4.1b

2357

2358 4.2.4 Uncertainty quantification

2359 A major component missing from many bathymetry inversions is assessing the spa-
2360 tially variable uncertainty in the resulting bathymetry depths. This uncertainty
2361 arises from a multitude of sources, including uncertainty in 1) the gravity data mea-
2362 surements, 2) constraint point depths, 3) user-defined variables, such as ice, water,
2363 or sediment density, and 4) uncertainties associated with the various methodologies
2364 of the inversion. Here we use a sampling-based approach to estimate the uncertainty,
2365 where the uncertainty of the *inputs* is used to assess the uncertainty of the *output*,
2366 in this case, the inverted bathymetry. This general method of uncertainty analysis
2367 is referred to as Monte Carlo sampling (Jansen et al., 1994).

2368

2369 For a generalized problem of inputs \mathbf{x} and a function $\mathbf{y}(\mathbf{x})$, Monte Carlo sim-
2370 ulation provides a means to answer the two following questions; 1) what is the
2371 uncertainty in $\mathbf{y}(\mathbf{x})$ given the uncertainty in \mathbf{x} ? and 2) what are the relative im-
2372 portance of the various components of \mathbf{x} with respect to $\mathbf{y}(\mathbf{x})$ (Helton et al., 2006)?
2373 While there are many components that contribute to the overall inversion uncer-
2374 tainty, here we will examine 1) uncertainty in the gravity data values, 2) depth
2375 uncertainty of the constraint points, 3) uncertainty in the chosen density values
2376 used for ice, water, and earth, and 4) uncertainties related to user-chosen parameter
2377 values in the inversion. Uncertainties that are not covered here as those which relate
2378 to processes of the inversion which don't have associated measurable input uncer-
2379 tainties. This includes the use of spatially non-variable density values for ice, water,
2380 or earth, or the effects of discretizing a real topographic surface as a series of prisms.

2381

2382 The Monte Carlo simulation consists of sampling the input parameters N times
2383 from their respective distributions (Figure 4.7b) and running the entire inversion
2384 workflow for each of the N parameter sets (Figure 4.7c). For each bathymetry grid
2385 cell, the weighted standard deviation of the N resulting inverted bathymetries is
2386 found (Figure 4.7d). This grid of ~~cell wise~~ (is ~~cell-specific~~ a better term here???)
2387 standard deviations show where the input parameters have a large effect on the
2388 bathymetry results. This grid is used as our estimate of the spatial uncertainty

in the inversion. The grid of cell-wise weighted median values is then taken to be the optimal inversion result. These cell-wise statistics are weighted by the inverse square of each inverted bathymetry's RMS difference with the constraint point depths (Figure 4.7d). This reduces the bias of inversions in the ensemble which performed poorly, as defined by not adhering to the constraints (Schnaidt & Heinson, 2015). To assess the relative importance of the input parameters, in addition to the complete Monte Carlo simulation, additional simulations are run where each parameter's effect is isolated. For these, only a singular parameter is sampled from its distribution, so that the resulting spatial standard deviation is due solely to the uncertainty of that parameter.

2399

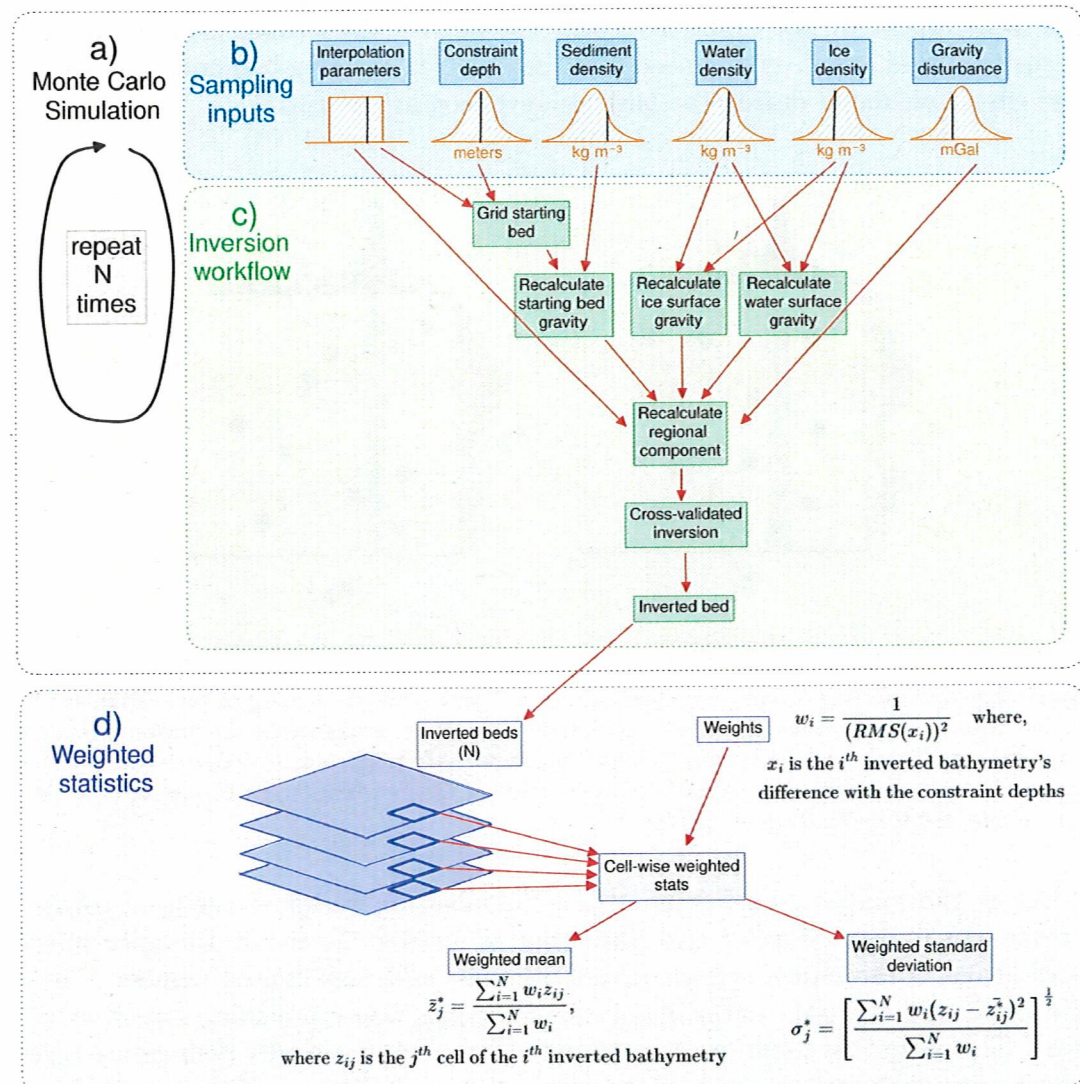


Figure 4.7: Schematic workflow diagram for the Monte Carlo uncertainty analysis. a) The Monte Carlo simulation, consisting of b) sampling the inputs from their respective distributions, and c) implementing the various components of the workflow, depending on which inputs have been sampled. This process is repeated N times, yielding N inverted bathymetry grids. d) Weighted cell-wise statistics are computed. Each inverted bathymetry grid (large purple boxes) is weighted by the respective inversion's constraint depth RMSE. These weights are used to compute the weighted mean and weighted standard deviation of each grid cell (bold purple square).

2400

The parameters included in the Monte Carlo sampling are; 1) the gravity dis-

turbance data, 2) the constraints point depths, 3) the gridding parameters to create the starting bathymetry, 4) the density of ice, 5) the density of water, 6) the density of sediment, and 7) gridding parameters for the constraint point minimization technique of regional gravity estimation (Figure 4.7b). For the full Monte Carlo simulation, with all the above inputs sampled from their respective distributions, the entire inversion workflow needs to be repeated with each of the N parameter sets. This includes 1) creating the starting bathymetry model from the constraint points (Section 4.2.3), 2) calculating the terrain mass effect to get the topo-free gravity disturbance (Section 4.2.1.2), 3) estimating the regional component of the disturbance and removing it (Section 4.2.1.3), and 4) running the damping parameter value cross-validation (Section 4.2.2) to obtain the inverted bathymetry (Figure 4.7). For the individual Monte Carlo simulations, only portions of this workflow need to be repeated. For example, if only the gravity disturbance is sampled, only the regional field and inversion need to be re-run. The starting bed and topographic mass effect calculated during the baseline inversion are re-used.

2416

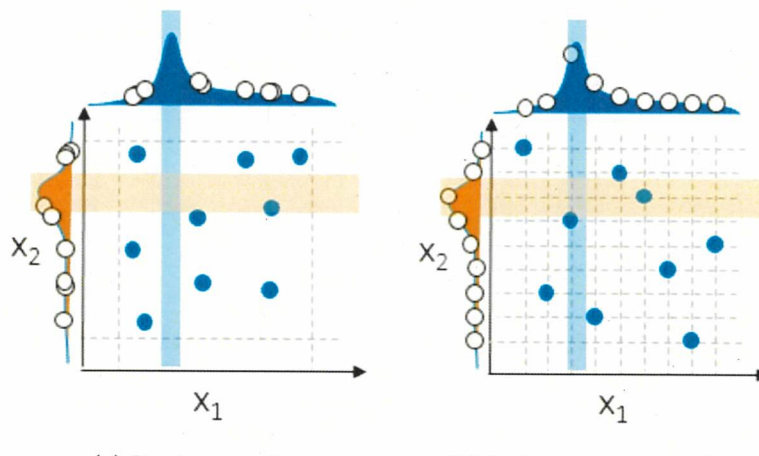


Figure 4.8: Comparison of sampling methods for a Monte Carlo simulation of two variables (X_1 and X_2) with 9 samples drawn from each. **a)** Random sampling, where values are drawn at random from each variable's distribution, and **b)** Latin hypercube sampling, where values are drawn from equal-probability intervals. Note the effective coverage of the distributions in **b** relative to **a**. The figure is adapted from Koch et al. (2017).

Due to the computational demand of a full inversion workflow, the total number of inversions in each Monte Carlo simulation is limited. To ensure the uncertainty distributions of the inputs are adequately sampled with this limited number of possible runs, we have used Latin hypercube sampling where possible (Jansen et al., 1994). This sampling technique is well suited for computationally demanding tasks since it ensures proper coverage of the uncertainty distributions of the sampled values, despite a low number of samples Helton et al., 2006. To accomplish this, for a Monte Carlo simulation of N runs, the given distributions are split into N intervals of equal probability and one value is chosen from each interval. The N values for each parameter are then randomly paired to get N sets of sampled input parameter values (Helton et al., 2006). Since the gravity data and constraint points are each sampled on a point-by-point basis, Latin hypercube sampling is unnecessary and random sampling is used. Figure 4.8 shows a $N = 9$ comparison of random sampling and Latin hypercube sampling for a two-parameter simulation.



2431

2432 4.3 Relation to past bathymetry inversions

2433 The fundamental theory in all bathymetry inversions is based on the fact that the
2434 density contrast across the bathymetry surface produces a measurable gravity ef-
2435 fect. This phenomenon gives rise to several techniques to convert observed gravity
2436 data into bathymetric depths. This by definition is a geophysical inverse problem
2437 (Oldenburg & Li, 2005), but the methods chosen to solve it vary from 3D rigorous
2438 inversions to iterative 2D forward modelling. Our inversion method follows a clas-
2439 sical least-squares approach to solving the inverse problem, while our uncertainty
2440 and sensitivity analysis follows a Bayesian approach (Aster et al., 2018). Here, we
2441 compare our inversion method and workflow to other bathymetry inversions. We
2442 attempt to include all past studies related to Antarctica, as well as several from
2443 Greenland. We start by comparing our technique for the gravity reduction process,
2444 followed by differences in the actual inversion, and finally by differences in our as-
2445 sessment of uncertainty.

2446

2447 4.3.1 Gravity reduction differences

2448 One of the largest differences between our method and past studies is the gravity
2449 reduction process. We employ a rigorous terrain mass effect calculation to obtain
2450 a topo-free gravity disturbance, often referred to as a Complete Bouguer Anomaly
2451 (Vajda et al., 2007). Theoretically, this gravity signal contains only effects due to
2452 subsurface density anomalies and inaccuracies in calculating the terrain mass effect.
2453 Our method isolates the gravity effect of this inaccuracy since it is due to the de-
2454 viations between the starting model of bathymetry and the true bathymetry. This
2455 is referred to as our residual component of the topo-free gravity disturbance. While
2456 most other bathymetry inversion studies achieve a similar residual anomaly, they
2457 complete this procedure in a theoretically different way, which may be introducing
2458 unnecessary errors. The differences arise from other studies ignoring the reference
2459 surface (the ellipsoid) for all calculations after the normal gravity correction.

2460

2461 The sign of a gravity disturbance value informs the interpreter as to whether
2462 the true Earth has either excess or deficient mass at that location with respect to
2463 the normal Earth. Therefore, the absolute level of gravity disturbance data should
2464 be retained, even though direct offsets (DC shifts) don't alter the amplitude of
2465 the gravity anomalies. For this reason, the reference surface used in the normal
2466 gravity calculation (here the ellipsoid) should be continued to be used in all further
2467 calculations of topographic masses, including in the forward calculation made during
2468 the inversion, as shown in Figure 4.5 b. Many studies instead have discretized the
2469 ice, water, and starting bathymetry surfaces into prism layers which either have
2470 arbitrary references or density values not relative to the normal Earth model. This
2471 alternative discretization is shown in Figure 4.5f-h. For example, the gravity effect
2472 of ice, if not just ignored (e.g., Yang et al., 2020b; Cochran & Bell, 2012; Jordan
2473 et al., 2020; Millan et al., 2017), is typically removed via a "stripping" technique
2474 (Vajda et al., 2008b), (e.g., Yang et al., 2021; Millan et al., 2020; Muto et al., 2013a;
2475 Greenbaum et al., 2015). This stripping involves calculating the forward gravity

Good tone

✓

of prisms with tops defined by the ice surface, bottoms defined by the ice base, and densities defined by the assumed density of ice (Figure 4.5f). Additionally, the prisms which comprise the starting bathymetry model for many inversions are bound above by the starting bathymetry, and below by an arbitrary constant depth (Figure 4.5h) (e.g., Tinto et al., 2019; Muto et al., 2013a). The forward gravity calculations of this style of discretization introduce several errors:

1. The largest of these errors is an offset in the mean value of the forward gravity relative to the observed gravity. This offset needs to be estimated and removed prior to comparison with the observed data. The DC-shift used to remove the offset is typically estimated by finding a value that minimizes the difference between the observed and predicted data at locations of known bathymetry (e.g., Eisermann et al., 2020; Cochran et al., 2020; Boghosian et al., 2015; Millan et al., 2017; Muto et al., 2013a; Constantino et al., 2020). This additional step, referred to as "pinning", is unnecessary in our implementation, due to adhering to a rigorous determination of the terrain mass effect. If an incorrect DC shift is applied, the significance of the zero level of the topo-free gravity disturbance is lost. The value of 0 signifies that the simplified model of the Earth (i.e. the starting bathymetry model) is equal to the true Earth density distribution. Shifting this zero-level due to errors in estimating the DC-shift may lead to a shift in the inverted bathymetry, especially if the inversion domain isn't well constrained. The DC-shifted terrain mass effect and the rigorous terrain mass effect for Antarctica are compared in Figure 4.6d.
2. The forward gravity calculation with this style of discretization results in slightly different amplitude anomalies compared to the true terrain mass effect. This difference is due to the different densities assigned to the prism layer between the two techniques (Figure 4.5). While this difference is likely below the range of uncertainties in the gravity error, it is an unnecessary addition of error to the gravity reduction process.
3. The last drawback to using this alternative discretization is an increased gravitational edge effect. As shown in Figure 4.5, the average densities and prism heights are larger with this technique. This increases the overall decay of calculated gravity at the edges of the model space, due to the contrast with the void-space beyond the model domain. To account for this, a larger buffer zone is needed, which can significantly increase the computational requirements during forward modelling (see Chapter 3 Section 3.2.2).

2511 Regional separation

2512 The last step in the gravity reduction process for bathymetry inversion is separating
 2513 the regional and residual signals, where the residual signal should theoretically be
 2514 entirely a result of the bathymetry surface. Some techniques commonly used for
 2515 this are described in Chapter 3 Section 3.2.4. Past bathymetry inversions have used
 2516 a variety of these techniques, as summarized below;

- 2517 1. Zero or uniform adjustment; For small inversion domains the regional field
 2518 is sometimes assumed to be minimal. In these scenarios, past studies have
 2519 either limited the inversion domain to where the regional field is assumed small
 2520 (Boghosian et al., 2015; Cochran & Bell, 2012), have used a uniform value for

*can
people
will
want to
know the
scale of that
in 2015?*

the regional component (Muto et al., 2013b), or have found a constant density value for the starting model which minimize the gravity misfit (Millan et al., 2017; Millan et al., 2018; An et al., 2017).

- 2524 2. Low-pass filtering; for inversion domains with an expected regional field slightly
2525 larger than the above scenario, low-pass filtering of the gravity data can ap-
2526 proximate the regional component (Eisermann et al., 2020; Hodgson et al.,
2527 2019).
- 2528 3. Geologic modelling; To account for the regional field, some studies create geo-
2529 logic models of varying density to estimate the regional field. These models are
2530 typically informed from other geophysical data (Hodgson et al., 2019; Green-
2531 baum et al., 2015), *a priori* geologic knowledge (Tinto & Bell, 2011; Con-
2532 stantino et al., 2020; Cochran et al., 2014), or from an approximated crustal
2533 density distribution (Tinto et al., 2019; Cochran et al., 2020; Eisermann et al.,
2534 2021; Wei et al., 2020).
- 2535 4. Upwards continuation / high altitude surveys; This technique estimates the
2536 long-wavelength regional component by either upward continuing the gravity
2537 data to large altitudes, using separate gravity data collect from high-altitude
2538 surveys (Muto et al., 2016), or a combination of both (Tinto et al., 2015)
- 2539 5. Constraint point minimization; the last commonly used technique, ~~referred to~~
2540 ~~in this study as constraint point minimization~~, utilizes the assumption that
2541 the desired residual component is near-zero at points of known bathymetry.
2542 From this assumption, the regional component at these constraints is entirely
2543 equal to the gravity anomaly value. To estimate the regional field, the gravity
2544 values are sampled at the constraints and interpolated over the region. This
2545 technique has been used in several recent inversions where sparse constraints
2546 are available (Yang et al., 2021; Millan et al., 2020; An et al., 2019a; Yang
2547 et al., 2020a; Jordan et al., 2020; An et al., 2019b; Vaňková et al., 2023).
2548 While implemented in a different method, this constraint point minimization
2549 follows the same concept as several studies which use the constrained locations
2550 to derive a spatially variable density model, accounting for the regional field
2551 (Tinto et al., 2019; Eisermann et al., 2021; Wei et al., 2020).

Tone is
good

2552 Here, we use the constraint point minimization technique for estimating and
2553 removing the regional component of the topo-free gravity disturbance.

2554 4.3.2 Inversion differences

2555 We have developed a conventional non-linear geometric gravity inversion algorithm,
2556 as often used in modelling density contrasts, such as sedimentary basins (e.g., Santos
2557 et al., 2015; Martins et al., 2010), or the Moho (e.g., Uieda & Barbosa, 2017;
2558 Pappa et al., 2019). This algorithm is similar in concept to inversions used in other
2559 bathymetric studies but differs in its implementation. Past inversion techniques
2560 used for bathymetry modelling can be grouped into several categories;

- 2561 1. algorithmic approaches. This method termed the "topographic shift method"
2562 (Hodgson et al., 2019; Jordan et al., 2020), while not a formal inversion,
2563 calculates the equivalent rock thickness from the residual component of gravity,

- 2564 adds this to the starting bathymetry model, and constrains the results by the
2565 locations of known bathymetry.
- 2566 2. 2D profile inversions. Using the method of Talwani et al. (1959), and often
2567 implemented within the commercial software Geosoft Oasis Montaj, these inv-
2568 ersions retain the 2D nature of the airborne flight lines and invert only along
2569 the path of the flight (Tinto et al., 2015; Tinto & Bell, 2011; Cochran et al.,
2570 2020; Boghosian et al., 2015; Cochran et al., 2014; Wei et al., 2020).
- 2571 3. 3D frequency-based inversions. This category of inversion uses a Fourier trans-
2572 formation to calculate the forward gravity effect of a continuous topographic
2573 surface, forgoing the need to discretize the topography into vertical prisms
2574 (Parker, 1972; Oldenburg, 1974). This Fourier transform is then iteratively
2575 modified to minimize the misfit to the observed gravity. This method, partic-
2576 ularly its implementation within the commercial software Geosoft Oasis
2577 Montaj, is frequently used for bathymetry inversions (Eisermann et al., 2020;
2578 Millan et al., 2020; An et al., 2019a; Cochran & Bell, 2012; Millan et al., 2017;
2579 Greenbaum et al., 2015; Millan et al., 2018; An et al., 2017; Eisermann et al.,
2580 2021; An et al., 2019b; Studinger et al., 2004).
- 2581 4. Simulated Annealing. This global optimization technique (Kirkpatrick et al.,
2582 1983) performs many forward calculations of possible bathymetry surfaces and
2583 slowly converges on a model which minimizes the misfit with the observations.
2584 This method, similar to our Monte Carlo uncertainty analysis, has the benefit
2585 of providing an uncertainty estimate of the resulting bathymetry based on the
2586 uncertainty in the inversion inputs. This has been used in several bathymetric
2587 inversions (Yang et al., 2021; Muto et al., 2016; Yang et al., 2020a; Muto et al.,
2588 2013a; Roy et al., 2005; Yang et al., 2018; Filina et al., 2008)
- 2589 5. Regularized least-squares inversions. This style of inversion is the conven-
2590 tional approach to solving non-unique inverse problems (Aster et al., 2018).
2591 While this method is commonly used for other geometric gravity inversions
2592 (e.g., Moho and basement), to our knowledge it is only applied to bathymetry
2593 inversions here, and in Vaňková et al. (2023).

2594 4.3.3 Uncertainty differences *analysis OR methods ?*

2595 Here we compare our uncertainty analysis to those from other bathymetry-gravity
2596 inversion studies. Most of these past studies provide an estimation of uncertainty,
2597 but only a few provide spatially variable uncertainties (e.g., An et al., 2019a; Muto
2598 et al., 2016). Typically, these inversion uncertainties are assumed to result from
2599 three sources.

- 2600 1. Uncertainty in the gravity data. The uncertainties resulting from the gravity
2601 data uncertainty are typically estimated using a Bouguer slab approximation,
2602 with an assumed density of the contrast between rock and water ($\sim 1600 \text{ kg m}^{-3}$), and a gravity uncertainty approximated from the RMS crossover values
2603 of the airborne gravity survey (e.g., Tinto et al., 2019; Boghosian et al., 2015;
2604 Constantino et al., 2020). Alternatively, a simple conversion factor has been
2605 proposed of 100 m of inversion uncertainty per 5 mGal of gravity uncertainty
2606 (An et al., 2019a; An et al., 2019b).

- 2608 2. Assumptions of the geologic structure. The uncertainty resulting from as-
 2609 sumptions of the geologic structure is typically simplified as uncertainties in
 2610 the choice of the constant density contrast between sediment and seawater.
 2611 This uncertainty is sometimes approximated as a ratio of change in density to
 2612 change in inverted relief as a percentage (e.g., $\sim 3\%$ relief for 50 kg m^{-3} Tinto
 2613 et al., 2019) or by altering the density and comparing the results (Boghosian
 2614 et al., 2015).
- 2615 3. Uncertainties in the past measurements of bathymetry (constraints). Lastly,
 2616 constraint point measurement uncertainties are typically assumed to result in a
 2617 1:1 uncertainty in the inverted bathymetry (e.g., Tinto et al., 2019; Boghosian
 2618 et al., 2015).

you
 don't detail
 your own
 approach here
 (but you
 do for the
 other summaries)

2619 4.4 Results

2620 Here we apply the above-described methods to recover a higher resolution bathymetry
 2621 beneath Antarctica's Ross Ice Shelf. First, we show the results from an individ-
 2622 ual workflow, as depicted in Figure 4.2. This includes the starting bathymetry
 2623 model, the topo-free gravity disturbance calculations, and the resulting inverted
 2624 bathymetry. Next, we present the Monte Carlo simulation results, where this entire
 2625 workflow is repeated many times with varying values of input data and parameters.

2626

2627 4.4.1 Starting bathymetry

2628 Existing options for a starting bathymetry model for the sub-Ross Ice Shelf in-
 2629 clude Bedmap2 (Fretwell et al., 2013) or BedMachine v3 (Morlighem et al., 2020;
 2630 Morlighem, 2022). BedMachine v3 for the Ross Ice Shelf contains the gravity-
 2631 inverted bathymetry results from Tinto et al. (2019). To avoid over-interpretation
 2632 of the gravity data (starting an inversion with the results of a separate inversion) we
 2633 opted to not use BedMachine for the starting model. Bedmap2 bed elevations for
 2634 the Ross Ice Shelf were created through the interpolation of the point constraints
 2635 (Fretwell et al., 2013). These point constraints within the ice shelf (Figure 4.1b)
 2636 were compiled from several surveys, including the early traverses of the 1950s and
 2637 60s (Crary, 1959; Crary et al., 1962; Crary & Robinson, 1962)³, and the Ross
 2638 Ice Shelf Geophysical and Glaciological Survey (RIGGS, 1973-1974 Bentley, 1984)
 2639 ($N = 223$). However, the gridding algorithm used (ArcGIS Topogrid), while pro-
 2640 ducing smooth results for the Ross Ice Shelf, didn't strictly adhere to the constraint
 2641 point depths. This can be seen through the comparison of constraint point depths
 2642 and Bedmap2 grid values at the same location (Figure 4.1b). The RMS difference
 2643 between the constraint depths and the grid depths within the ice shelf is 138 m.
 2644 The largest differences are concentrated along the Transantarctic Mountain Front,
 2645 where Bedmap2 grid values are much shallower than the constraint points. Due to
 2646 this over-smoothing of the constraints, we have opted to create our own starting
 2647 bathymetry model.

2648

³These surveys included the Ross Ice Shelf Traverse (1957-1958), the Little America Station Byrd Trail Traverse (1958), the Victoria Land Traverse (1958-1959), and the Discovery Deep Traverse (1960), see Bennett (1964) for the data and descriptions.

This model was created from the combination of various seismic survey constraint points on the ice shelf, and bed data from BedMachine v3 (Morlighem et al., 2020; Morlighem, 2022) outside of the ice shelf. To create this, the BedMachine v3 bed elevations, relative to the WGS-84 ellipsoid, were masked within the Ross Ice Shelf, based on the MEaSUREs v2 Ross Ice Shelf boundary (Mouginot et al., 2017; Rignot et al., 2013). This data ^{These were} was converted from gridded data into point data and merged with the various bathymetry data within the ice shelf. A continuous grid of bathymetry depths at a 5 km cell size was then interpolated from the combined data inside and outside the shelf. The interpolation can be accomplished with two gridding methods, bi-harmonic splines (Sandwell, 1987), and minimum curvature (Smith & Wessel, 1990). While the bi-harmonic spline method appears to have several advantages over minimum curvature (Chapter 3 Section 3.4.2), such as the ability to apply weights to the data, interpolating the above Ross Ice Shelf data resulted in significant unconstrained minima and maxima. Initial inversion results showed these erroneous features carry through to the final inverted bathymetry. Due to this, we have opted to interpolate the data to create the starting bathymetry model using tensioned minimum curvature. This method resulted in less extreme un-constrained minima and maxima.

2667

To test the importance of the tension value used in the minimum curvature gridding, we performed 6 interpolations, with tension values of 0, 0.2, 0.4, 0.6, 0.8, and 1 (Figure 4.9a-f). From these six resulting bathymetry models, we calculated the standard deviation (Figure 4.9g) and the cell-wise mean (Figure 4.9h). These statistics were weighted, in the same method described in Figure 4.7d. The weight value used for each grid was the inverse square of the RMS difference between the constraint point depth values and the resulting grid values at the same points. These RMS values are shown in the figure titles of Figure 4.9a-f. This weighted mean starting model is compared to Bedmap2 bathymetry (Figure 4.9i). Note that while low tension factors result in models that closely match the constraints, they also produce local maxima and minima away from the data, which is not ideal since these features can be seen to carry through the inversion to the final bathymetry, as discussed later. Alternatively, higher tension values produce models that don't match the constraints as well (higher RMS values), but they don't have as many erroneous features. For this reason, we use the cell-wise mean of the six models as our starting bathymetry (Figure 4.9h). This model has an RMS difference from BedMap2 within the ice shelf of 95 m.

2685

From these constraint points used to create the starting bathymetry, a weighting grid was created (Figure 4.10). This grid was calculated from the distance between each grid cell and the nearest constraint point. This minimum constraint distance (top annotations of Figure 4.10 colorbar) was then normalized between 0 and 1 to create the weighting grid (bottom annotations of Figure 4.10 colorbar). As all grid cells outside of the ice shelf border are considered constraint points non-zero weights and minimum constraint distances are confined to within the ice shelf border. The colorbar histogram shows a mean minimum constraint distance within the ice shelf of approximately 20 km, and an upper limit of approximately 60 km. Within the shelf, there are 223 constraint points. Over an area of $\sim 480,000 \text{ km}^2$ (Mouginot et al., 2017), this equates to a constraint density of ~ 1 constraint per 2154 km^2 .

2697

46 x 46 km

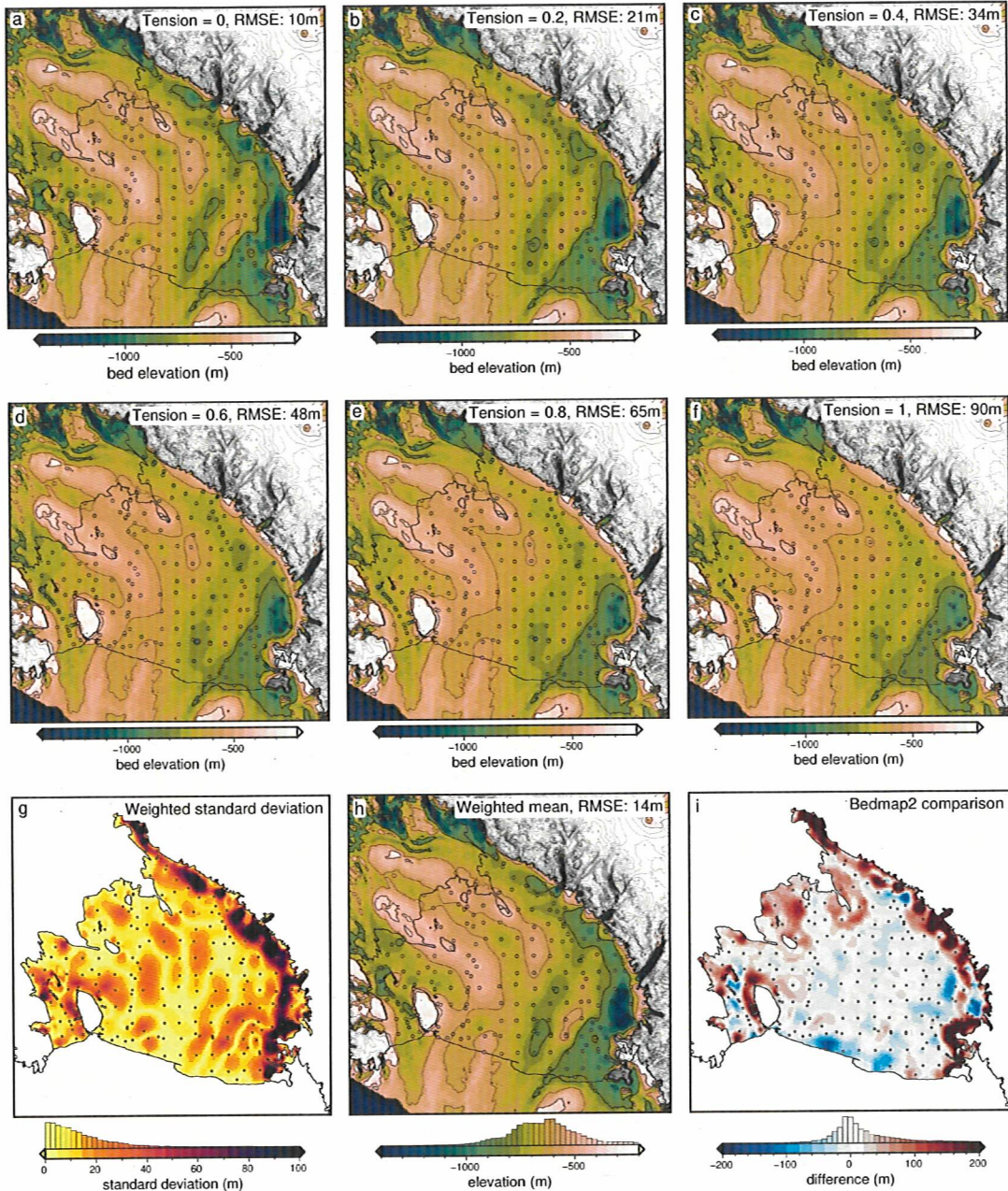


Figure 4.9: Starting bathymetry models from the interpolation of constraint points within the ice shelf and BedMachine v3 gridded data outside of the shelf (Morlighem et al., 2020; Morlighem, 2022). The ice shelf border, from Mouginot et al. (2017), is shown as the solid black line, representing the grounding line and the calving front. **a-f**) Bathymetry models resulting from 6 varying tension factor values of minimum curvature interpolation. Contours shown at 400m intervals. **g)** The cell-wise weighted standard deviation of the six models (**a-f**). **h)** The cell-wise weighted mean bed elevation from the six models. **i)** The difference between Bedmap2 bathymetry and the mean model (**h**). The RMS difference is 95 m. Blues show where the mean model is shallower than Bedmap2, while reds show where the mean model is deeper. Root mean square error (RMSE) values in the plot titles are between the constraint point depths and the values at those points on the interpolated grids.

2698 4.4.2 Gravity processing results

2699 We use airborne gravity data from the Ross Ocean and ice Shelf Environment, and
2700 Tectonic setting Through Aerogeophysical surveys and modelling project (ROSETTA-

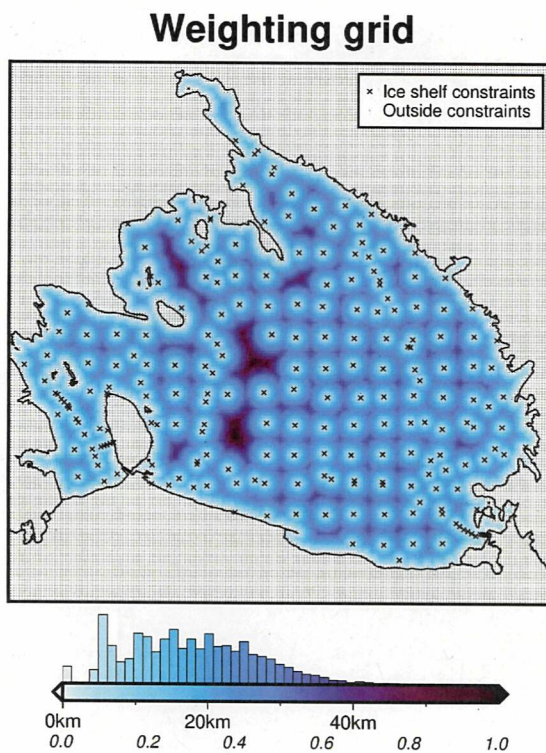


Figure 4.10: Weighting grid used in the Ross Ice Shelf bathymetry inversion. Grid colors show both the distance between each grid cell and the nearest constraint point and the weight values (0 - 1) from the normalization of these distances. Constraint points are defined as either direct measurements of bathymetry within the ice shelf (black crosses), or any grid cell outside of the ice shelf (small black dots). The ice shelf border, from Mouginot et al. (2017) is shown as the solid black line, representing the grounding line or the calving front.

2701 Ice). This project was created with the goal of investigating the interactions between
 2702 ice, ocean, and earth of Antarctica's Ross Ice Shelf (Tinto et al., 2019). The survey
 2703 consisted of 3 field seasons (2015-2017) of airborne geophysical surveying with a
 2704 survey design consisting of E-W flight lines, at a nominal spacing of 10 km, and
 2705 N-S tie lines with a nominal spacing of 55 km (Figure 4.1a). Flights were flown
 2706 at an average of 750 m above the ice surface and a speed of 180 knots (93 ms^{-1}),
 2707 The survey was designed to maximize the overlap between the flight lines and the
 2708 past bathymetry constraints across the ice shelf from the RIGGS seismic surveys
 2709 (Bentley, 1984). The data collection and initial processing were performed by Tinto
 2710 et al. (2019) and are briefly summarized here. The gravity data were collected with
 2711 a combination of a ZLS gravimeter, an iMAR inertial measurement unit, and a DgS
 2712 gravimeter. The ZLS data was tied to an absolute gravity reference station at Mc-
 2713 Murdo Station. Poor-quality data from the ZLS was replaced with the iMAR or
 2714 DgS values. The accelerations of the aircraft were calculated from GPS data and
 2715 removed from the gravity signal. The Eötvös correction was applied, to account
 2716 for measuring gravity on a moving platform (Harlan, 1968). At each observation
 2717 point, the effects of the normal earth were calculated and removed, giving the grav-
 2718 ity disturbance values (See Section 4.2.1.1). Levelling was then performed using the
 2719 cross-over values between E-W flight lines and N-S tie lines.

2720

2721 Since this bathymetry inversion is strongly influenced by noise in the gravity
 2722 data, as demonstrated in Chapter 3 Section 3.9, we have performed additional pro-

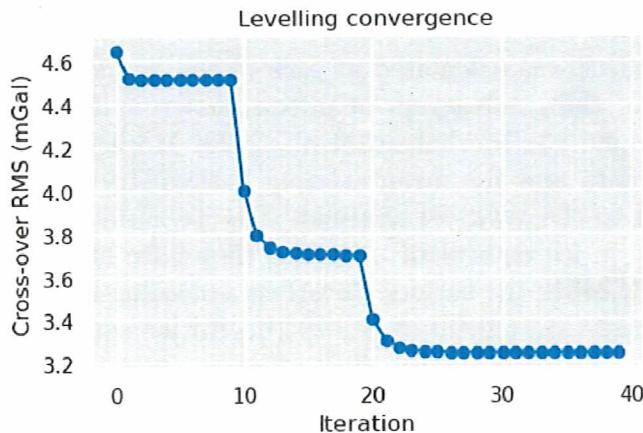


Figure 4.11: Re-leveelling of the ROSETTA-Ice gravity data. First, flight lines were individually upward continued, then cross-over point mis-ties were found. These were used in 0th, 1st, and 2nd order iterative levelling, alternative between levelling flight lines to tie lines and vice versa at each iteration. The RMS cross-over errors at each iteration are shown. The major steps show the 0th, 1st, and 2nd order stages of levelling.

cessing to the published ROSETTA-Ice dataset. Erroneous sections of flight line data were manually removed, and the dataset was re-levelled. The levelling procedure utilizes the gravity difference between E-W and N-S flight lines at cross-over points. While the flight paths intersect in 2-D space, their altitudes typically differ, meaning there is no true cross-over point in 3-D space. To account for this, the flight lines are individually upward continued to a constant elevation of 1 km (ellipsoidal height). The mean elevation of the cleaned data was \sim 790 m, and 1 km was greater than 96% of the data. This limited the amount of downward continuation while retaining a spatial resolution close to the original data. This continuation was calculated using the equivalent source technique (see Section 3.3.1 Soler & Uieda, 2021; Dampney, 1969). Since the cross-over points are now true 3-D intersections, the difference between E-W and N-S lines at these points (mis-ties) can be used to re-level the dataset. Here, we alternate between levelling the E-W lines to the N-S lines, and vice versa. We start with a 0-th order levelling, where only DC shifts are applied. Followed by a 1st and 2nd order levelling, where 1 and 2-degree polynomials, respectively, are fit to the mis-ties, and used to level the lines. The results of this levelling procedure are shown in Figure 4.11. For each order of levelling several iterations are performed. The step-wise convergence of the RMS mis-tie values shows the 0th, 1st, and 2nd order levelling stages. The re-leveelling procedure brought the RMS mis-tie from \sim 4.8 mGal to \sim 3.2 mGal.

Finally, this re-levelled gravity disturbance line data were gridded onto a regular grid at 2.5 km spacing, using equivalent sources. Since the inversion only affects the bathymetry within the ice shelf border, as implemented with the weighting grid (Figure 4.10), the interpolated gravity grid is masked beyond 10 km outside of the ice shelf border (Figure 4.11b). This 2.5 km gridded data ($N = 85,914$) consists of both the *testing* ($N = 64,435$) and *training* ($N = 21,479$) sets used in the cross-validation. With the grid configuration shown in Chapter 3 Figure 3.4, the *training* data used in the actual inversion are on a regular 5 km grid.

✓

Finally, this re-levelled gravity disturbance line data were gridded onto a regular grid at 2.5 km spacing, using equivalent sources. Since the inversion only affects the bathymetry within the ice shelf border, as implemented with the weighting grid (Figure 4.10), the interpolated gravity grid is masked beyond 10 km outside of the ice shelf border (Figure 4.11b). This 2.5 km gridded data ($N = 85,914$) consists of both the *testing* ($N = 64,435$) and *training* ($N = 21,479$) sets used in the cross-validation. With the grid configuration shown in Chapter 3 Figure 3.4, the *training* data used in the actual inversion are on a regular 5 km grid.

2752

4.4.3 Gravity reduction results

The terrain mass effect was calculated at each of the gridded gravity data points. For this calculation, the three layers of prisms shown in Figure 4.5c-e were created from BedMachine v3 (Morlighem et al., 2020; Morlighem, 2022) ice surface and water surface data and the mean starting bathymetry from Figure 4.9h. All data are referenced to the WGS-84 ellipsoid. The ice surface elevations used from BedMachine v3 are in ice equivalent, meaning they have had a firn depth correction applied, *making for* slightly lower the surface elevations according to account for spatially variable firn thickness (Morlighem et al., 2020). An ice equivalent surface is suitable for calculating the terrain mass effect, since it gives the estimated thickness of the ice shelf with a density of ice, instead of the true ice shelf thickness, with a layer of low density firn above. Comparing the forward gravity calculated from the true geometry of ice shelf thickness, the ice equivalent thickness, and a 2-layer model with firn and ice, show minimal differences, and thus we use the ice equivalent thickness in the terrain mass effect. The densities used in the terrain mass effect calculations were 1 kg m⁻³ for air, 915 kg m⁻³ for the density of ice, 1024 kg m⁻³ for the density of Ross Ice Shelf sea water (Griggs & Bamber, 2011), and 2300 kg m⁻³ for the density of the seafloor. The inversion domain was 1 million km² (1000 km × 1000 km). To avoid gravitational edge effects in the forward calculations, the prism layers were extended in all directions by a 40 km buffer zone, resulting in 120,000 prisms. The resulting terrain mass effect was subtracted from the gravity disturbance to get the topo-free gravity disturbance. These data are shown in Figure 4.12.

The topo-free gravity disturbance was subsequently separated into the regional and residual components. This was accomplished with constraint point minimization (Chapter 3 Section 3.2.4). While the synthetic data of the past chapter showed a clear benefit of using a bi-harmonic spline interpolation over a minimum curvature interpolation, we use minimum curvature here. As with the interpolation for the starting bathymetry model, bi-harmonic spline interpolation led to excessive unconstrained maximum or minima. The resulting regional and residual components are shown in Figure 4.12.

4.4.4 Inversion results

With the residual component of the topo-free gravity disturbance as the inversion input (Figure 4.12d), we ran 10 inversions with varying levels of damping. Each inversion used a density of 1024 kg m⁻³ for ocean water and 2300 kg m⁻³ for the density of the seafloor. For each value of the damping parameter, the cross-validation score was calculated by forward modelling the gravity effect of the resulting bathymetry model onto the locations of the testing gravity data. The RMS difference between the residual component of the topo-free gravity disturbance and the forward-modelled results at these testing points gave the score. These scores are shown in Figure 4.13a. The lowest score was achieved with a damping value of 10⁻².

This inversion took 8 iterations and 135 seconds and converged due to a lack of change in the ℓ^2 -norm between subsequent iterations (Figure 4.13b). The RMS of the residual gravity started at 6.1 mGal prior to the inversion and was reduced to 4.0 mGal (Fig 4.13b).

time
is
how
spec
useful
of capture
area

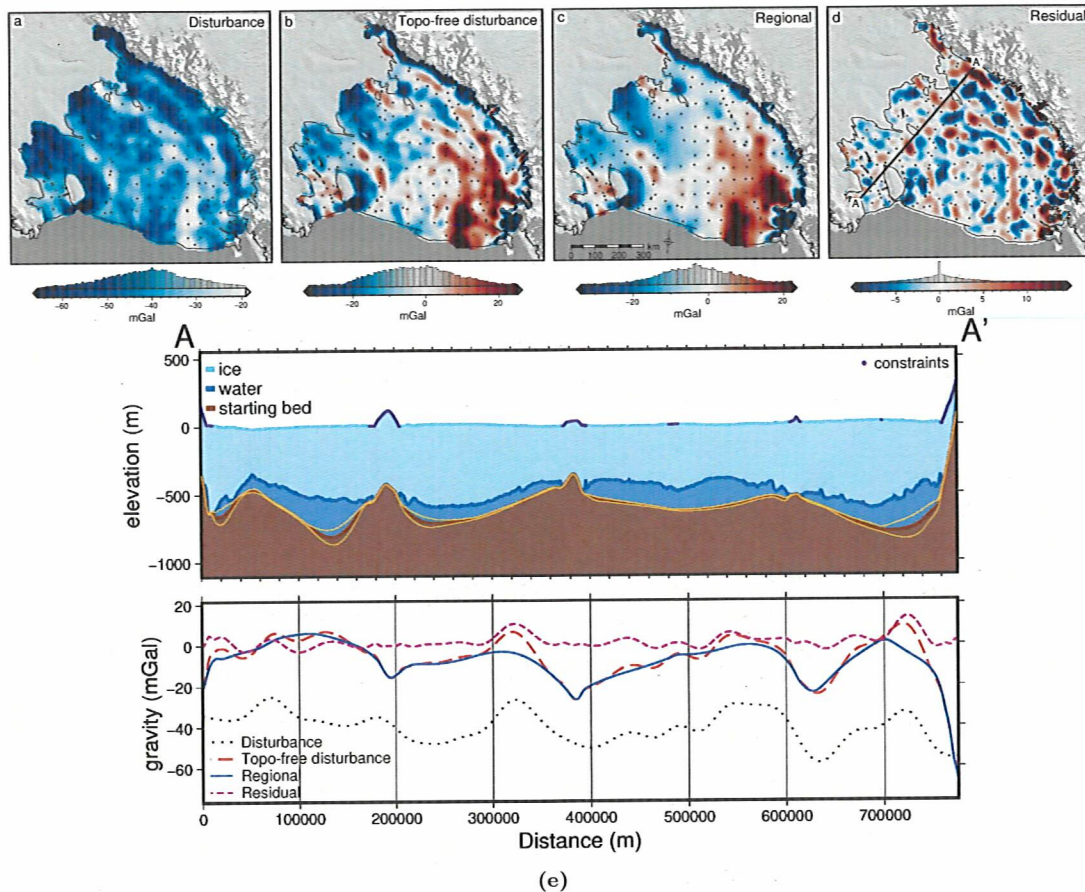


Figure 4.12: Gravity reduction results for the Ross Ice Shelf. **a)** Gravity disturbance, **b)** topo-free gravity disturbance, after the removal of the terrain mass effect, **c)** regional component of the topo-free disturbance, estimated with constraint point minimization, and **d)** residual component of the topo-free disturbance, as the difference between **b** and **c**. Background imagery is from MODIS-MOA (Scambos et al., 2007) and grounding line and coastlines are from (Morlighem, 2022). Constraint points within the ice shelf are shown as dots. **e)** Profile from A to A', location shown in **d**. **Upper panel** shows cross-section, with ice surface and ice base from BedMachine v3 (Morlighem et al., 2020; Morlighem, 2022). Brown layer shows the mean starting bed model with bounding uncertainty (light brown lines) from the standard deviation of the various starting bed models in Figure 4.9. Purple points along the ice surface show locations within 5 km of a constraint point or grounded ice. **Lower panel** shows data from **a-d** along the profile.

2800
 2801 The inverted bathymetry model for the sub-Ross Ice Shelf, at a 5km resolution,
 2802 is shown in Figure 4.13c. Note that this is just the result of a single inversion. Our
 final actually inverted bathymetry model is achieved through the Monte Carlo simu-
 2803 lation, as described below. The RMS difference between the inversion results and the
 2804 starting model at the constraints is 16 m. The thickness of the water column (ocean
 2805 draft), defined as the difference between BedMachine v3 icebase and the inverted
 2806 bathymetry, is shown in Figure 4.13d.
 2807
 2808

2809 4.4.5 Uncertainty

2810 We used a series of Monte Carlo simulations (Figure 4.7) to assess both the spatial
 2811 uncertainty of the resulting inverted bathymetry and the importance of the various

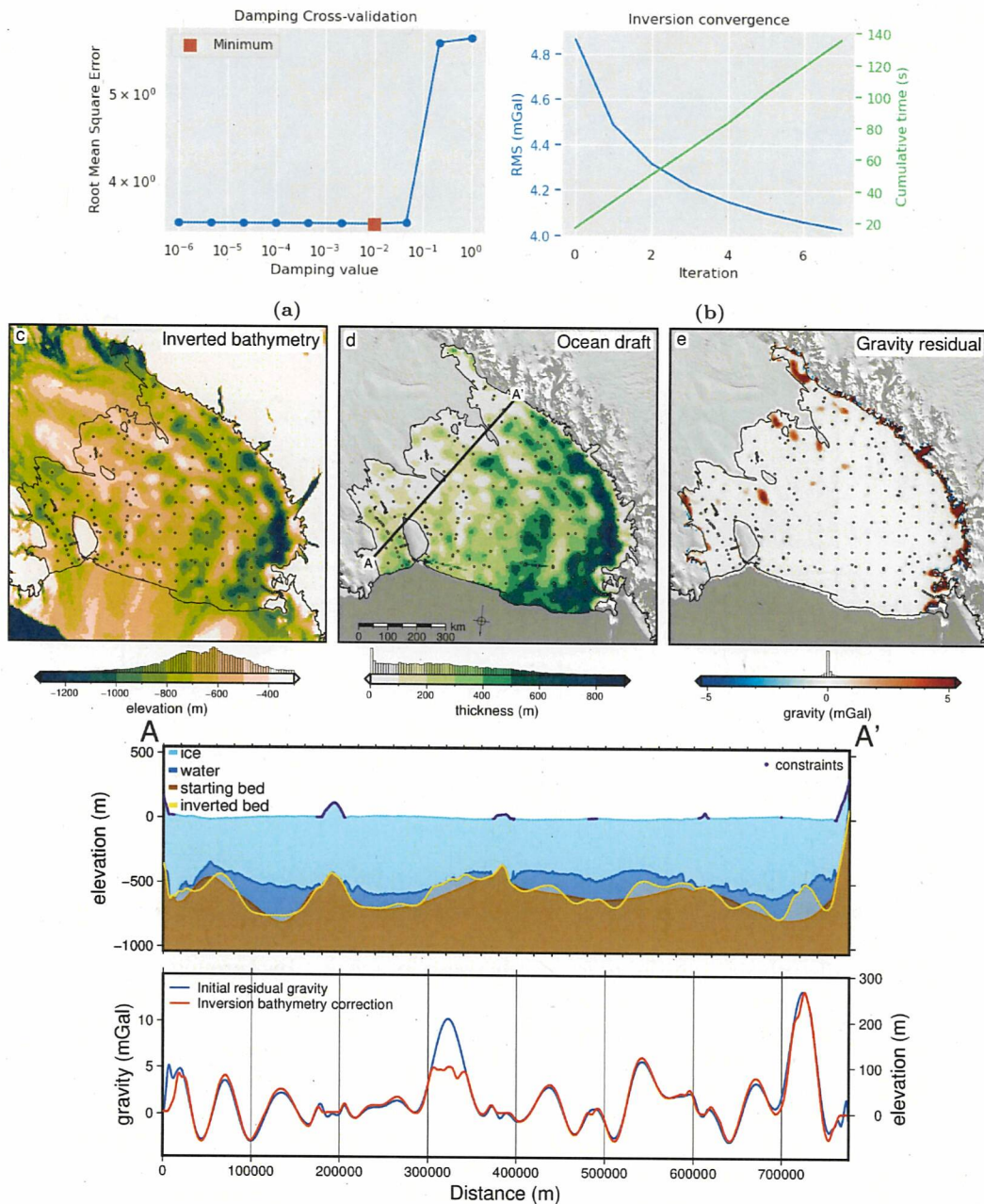


Figure 4.13: Ross Ice Shelf singular bathymetry inversion results. **a)** Damping parameter cross-validation with the lowest score shown in red. **b)** Convergence curve and cumulative inversion time for the optimal inversion. Blue line (left y-axis) shows consecutive iteration's RMS residual component of the topo-free gravity disturbance. Green line (right y-axis) shows cumulative time to run the inversion. **c)** Inverted bathymetry, **d)** ocean draft (water column thickness) between the inverted bathymetry and BedMachine v3 icebase (Morlighem et al., 2020; Morlighem, 2022), **e)** final residual component of the topo-free gravity disturbance. **Profile A to A'**. **Upper panel** shows ice surface and icebase from BedMachine v3, both the starting bathymetry (dark brown) and the inverted bathymetry (light brown). Locations within 5 km of a constraint point or grounded ice are shown in purple along the ice surface. **Lower panel** shows the initial residual gravity used as input to the inversion (blue line, left y-axis), and the total correction (red line, right y-axis) applied to the starting bathymetry surface during the inversion to get the inverted bathymetry.

2812 components and parameters of the inversion. By varying the inputs of the inversion
 2813 within their ranges of uncertainties, we can gather a range of the possible bathymetry
 2814 results, which when compared shows where the inversion results are more or less

2815 certain. The inputs and their respective uncertainty distributions included in the
2816 sampling are:

- 2817 1. gravity disturbance data, sampled from a normal distribution with a mean of
2818 the data point, and a standard deviation of the RMS mis-tie of the line data
2819 after levelling (3.3 mGal),
- 2820 2. constraint point depths, sampled from a normal distribution with a mean of
2821 the measured depth, and a standard deviation of 10 m for points outside of
2822 the ice shelf, and 5% of depth from the ice surface for points within the ice
2823 shelf (mean of 36 m),
Don't go above 917 - okay if you already have.
- 2824 3. the density of ice, water, and sediment, all from normal distributions with
2825 means of 915 kg m^{-3} , 1024 kg m^{-3} , and 2300 kg m^{-3} respectively, and standard
2826 deviations of 5 kg m^{-3} , 5 kg m^{-3} , and 400 kg m^{-3} . The small standard deviations
2827 of ice and water compared to sediment reflects the relative certainty of the
2828 value and spatial heterogeneity of the density of ice and water, compared to
2829 those of the material comprising the sea floor. For the Ross Ice Shelf, the entire
2830 region is likely to be draped is at least 10's of meters of sediment (Chapter 2,
2831 Tankersley et al., 2022). With a mean of 2300 kg m^{-3} and a standard deviation
2832 of 400 kg m^{-3} , these values span the range from unconsolidated sediment to
2833 low-density crystalline rock (Schön, 2015).
- 2834 4. the tension factor used in minimum curvature gridding for interpolating both
2835 the starting bathymetry model and the regional component of gravity. The
2836 tension factor values were sampled from a uniform distribution between 0 and
2837 1.

2838 Figure 4.14 shows the results of the Latin hypercube sampling of the 5 input
2839 variables (not including the gravity and constraints data). The correlations between
2840 each set of variables show that pairwise correlation was minimal. This is ideal since
2841 these inputs are unrelated, and therefore their sampled values should be uncorre-
2842 lated (Helton et al., 2006). This also shows that with only 10 samplings, the Latin
2843 hypercube sampling was able to provide adequate spatial coverage of the individual
2844 distributions (4.14b) as well as all the pairwise distributions combinations (4.14a). ✓

2845 Each simulation consisted of 10 runs. We performed a *full* simulation, where
2846 each of the above inputs were sampled (Figure 4.15). We performed five additional
2847 simulations (Figure 4.16) where 1) only the gravity data was sampled, 2) only the
2848 constraint point depths were sampled, 3) only the density values of ice, water, and
2849 sediment were sampled, 4) only the tension factor for interpolating the starting
2850 bathymetry model was sampled, and finally 5) only the tension factor for interpo-
2851 lating the regional component of gravity was sampled. Each simulation results in a
2852 series of inverted bathymetries. Finding the cell-wise weighted standard deviation of
2853 the bathymetry depths for each of these simulations gives an estimation of the un-
2854 certainty resulting from the associated parameter. The cell-wise statistics of these
2855 simulations were low-pass filtered to remove high-frequency noise induced by the
2856 random sampling. For the full simulation (Figure 4.15b) the weighted mean of the
2857 resulting bathymetries gives the final inverted bathymetry results of this study (Fig-
2858 ure 4.15a). Note that this final bathymetry model resulting from the Monte Carlo
2859 simulation is similar, but distinct from the inverted bathymetry resulting from a

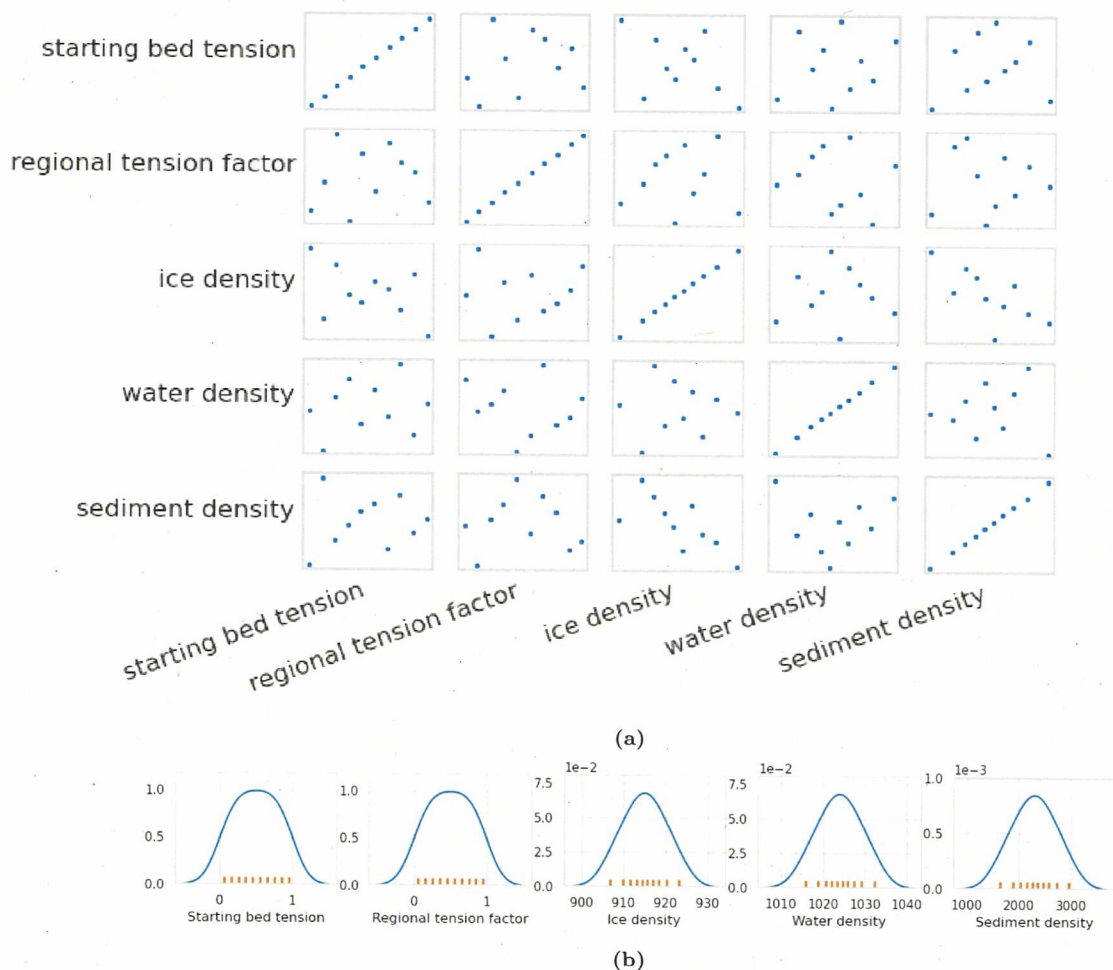


Figure 4.14: Latin hypercube sampling results for the 10 inversions of the full Monte Carlo simulation. **a)** Correlations between each pair of the 5 sampled input parameters. **b)** Resulting distributions of the 10 sampled values of each parameter. Blue line shows kernel density estimates fit to each set of sampled values, which are shown as orange ticks.

2860 single inversion without the Monte Carlo simulation, shown in Figure 4.13c.

2861

2862 The final bathymetry and uncertainty grids were resampled to a resolution of
 2863 500 m, from their original 5 km resolutions, masked outside of the ice shelf, and
 2864 merged to the 500 m resolution bed and uncertainty data of BedMachine v3. This
 2865 final bathymetry has a mean elevation of ~ 700 m within the ice shelf. The deepest
 2866 point is $\sim -1370 \pm 187$ m, located near the Byrd Glacier outlet (Figure 4.1b).
 2867 Bathymetric features appear to have continuity with features from BedMachine v3
 2868 data outside of the ice shelf. The RMS difference between the bathymetry and the
 2869 original constraint point depths is 44 m. Subtracting the bathymetry from the ice
 2870 base elevations of BedMachine v3 (Morlighem et al., 2020; Morlighem, 2022) gives
 2871 the ocean draft, as shown in Figure 4.18b. Without ice base uncertainty estimates
 2872 from BedMachine v3, we use the bathymetry uncertainty as our uncertainty for the
 2873 ocean draft, acknowledging that this is a minimum uncertainty. Within the ice shelf
 2874 boundary, this water column thickness has a mean value of 260 m and a maximum
 2875 of 1000 m, located near the Nimrod Glacier outlet. Here, the bathymetry has an un-
 2876 certainty of ± 800 m. Outside of this region, the thickest ocean cavity is $\sim 940 \pm 180$

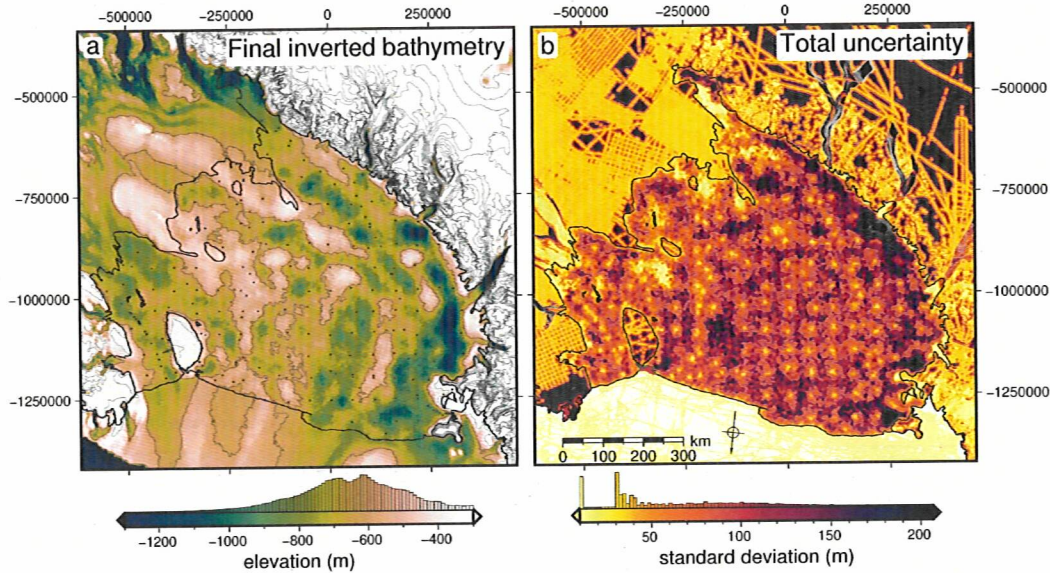


Figure 4.15: Final bathymetry depths and uncertainties from the full Monte Carlo simulation, merged with 500m resolution elevation and uncertainty data outside of the shelf from BedMachine v3 (Morlighem et al., 2020; Morlighem, 2022). **a)** Final inverted bathymetry model, calculated as the weighted mean of the full Monte Carlo simulation. Shown with 300 m contours. **b)** Uncertainty estimation of the inverted bathymetry results from the cell-wise weighted standard deviation of the inverted bathymetry results from the full Monte Carlo simulation. Shown with 100 m contours. Constraints within the ice shelf are shown as dots in **a**. Grounding line and coastline are shown in black (Morlighem, 2022). Background imagery is from Scambos et al. (2007).

2877 m, located at the Byrd Glacier outlet. The similarity between the bathymetry depth
 2878 and the ocean draft shows that the draft is predominantly controlled by bathymetry
 2879 and that the ice base topography is smooth compared to the bed. The uncertainty
 2880 in the bed elevation ranges from \sim 10 - 850 m, with a mean of 95 m (Figure 4.13b).
 2881 It has an approximately normal distribution, with a slight skew to the higher values.
 2882 In general, the uncertainty is lowest at the constraint points and highest far from
 2883 constraints. There are elevated uncertainties in several spots, with the largest being
 2884 along the Transantarctic mountain front.

2885 Subheadings: Partitioning uncertainty. (or similar)

2886 The uncertainty in the inverted bathymetry which arises from the uncertainty in
 2887 gravity data (Figure 4.16a) is relatively spatially uniform, with a mean of 85 m. It
 2888 is lowest immediately at the constraints, and generally highest far from constraints.
 2889 The uncertainty from the constraints point depths (Figure 4.16b) is also generally
 2890 spatially uniform, with a mean of 9 m. Conversely, it is highest at the constraints,
 2891 and lowest far from constraints. The uncertainty resulting from the choice of den-
 2892 sity values (Figure 4.16c) displays a more heterogenous spatial distribution than the
 2893 previous two uncertainties. It is lowest at the constraints and has a mean of 24 m.
 2894 The largest values are located at the gaps between constraints. The uncertainty
 2895 resulting from the interpolation of the starting bed (Figure 4.16d) has a distinct
 2896 spatial distribution. It is highest along the Transantarctic mountain front, with val-
 2897 ues up to 40 m, but it has an overall mean of 7 m. Lastly, the uncertainty resulting
 2898 from the estimation and removal of the regional component of gravity, prior to the
 2899 inversion, (Figure 4.16e), also shows highest values along the mountain front, with
 2900 values over 200 m (up to 700 m at the Nimrod Glacier outlet). The mean value is
 2901 24 m. The reported uncertainties and their components from a wide range of past

Repetition

I got it

on re-read.

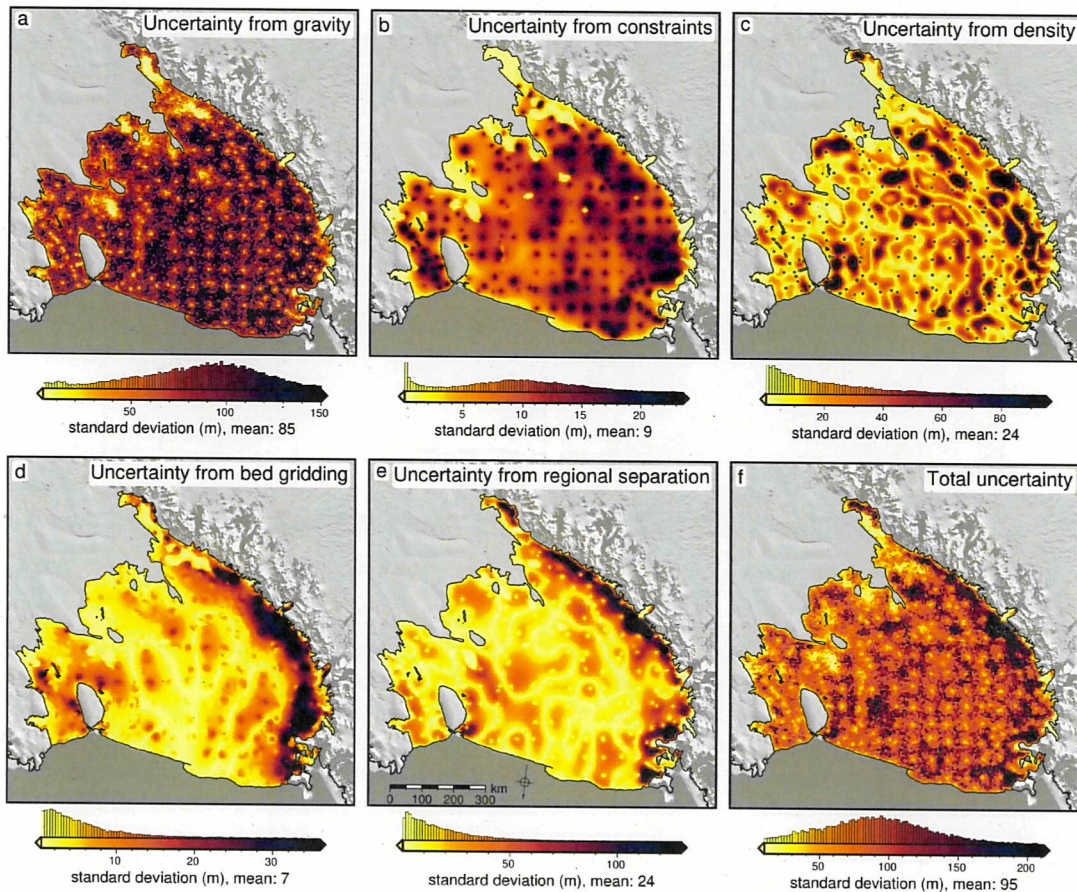


Figure 4.16: Sensitivity analysis for the inversion input data and parameters. Cell-wise weighted standard deviations of the inverted bathymetry results from Monte Carlo simulations with sampling the uncertainties of the a) gravity data, b) constraint points depths, c) ice, water, and sediment density values, d) starting bed interpolation tension factor, and e) tension factor for interpolating the regional gravity component. f) The total uncertainty from the full simulation. 100 m contours in white. Constraints within the ice shelf are shown as dots in c). Grounding line and coastline shown in black (Morlighem, 2022). Background imagery is from Scambos et al. (2007).

2902 studies are shown in Table 4.1.

2903

2904 4.5 Discussion

2905 Here we discuss the results of the updated Ross Ice Shelf bathymetry model from the
 2906 inversion of airborne gravity data. First, we describe the results of the uncertainty
 2907 and parameter sensitivity analysis. Then we compare our results with two past
 2908 bathymetry models beneath the Ross Ice Shelf and discuss the differences. Lastly,
 2909 we discuss various implications of this updated bathymetry model, including how
 2910 the findings relate to geology, tectonics, and ice sheet dynamics.

2911 4.5.1 Uncertainties and parameter importance

2912 The results of our Monte Carlo simulations provide answers to several important
 2913 questions; 1) how confident are we in the inverted bathymetry depths? 2) where
 2914 are we most and least confident about the bathymetry depth? 3) what are the

mean range
show
of dr

Study	total	Inverted bathymetry uncertainty (m)			Comments
		from gravity	from geology	from constraints	
This study	95	85	48 (24+24)	9	
Eisermann et al. (2021)	220	84	116	20	
Tinto et al. (2015)	160	26	124	10	
Constantino et al. (2020)	133	34	90	5-10	
Boghosian et al. (2015)	110	10-28	50-70	10	
Tinto and Bell (2011)	70	34	10-15	20	
Tinto et al. (2019)	68	48	10	10	
Eisermann et al. (2020)	175-225	-	-	10	
Jordan et al. (2020)	100	23	-	-	
An et al. (2019a)	60	60	-	-	
Studinger et al. (2004)	250	-	-	-	
Wei et al. (2020)	246	-	-	-	
Greenbaum et al. (2015)	190	-	-	-	
Brisbourne et al. (2014)	160	-	-	-	
Hodgson et al. (2019)	100	-	-	-	
Yang et al. (2021)	68	-	-	-	
An et al. (2017)	60	-	-	-	
Millan et al. (2017)	50-65	-	-	-	
Millan et al. (2018)	30-50	-	-	-	
Millan et al. (2020)	45	-	-	-	
Filina et al. (2008)	-	19	-	-	
Mean		119 (<i>N</i> = 23)	41 (<i>N</i> = 11)	59 (<i>N</i> = 9)	12 (<i>N</i> = 9)

Table 4.1: Reported inverted bathymetry uncertainties and the various components.

2915 specific sources of this uncertainty? and finally, 4) what can be done to limit the
2916 uncertainty? Figures 4.15b and 4.16f show the resulting spatial uncertainty of the
2917 inverted bathymetry, providing an answer to the first two questions. To determine
2918 the sources of this uncertainty, the individual inputs to the inversion were isolated
2919 and their effects on the estimated uncertainty were found (Figure 4.16).

2920

2921 Gravity component

2922 The largest contributor to the overall uncertainty of the inversion is the uncertainty
2923 of the gravity data (Figure 4.16a). This uncertainty resulting from the gravity data
2924 results in a base-level bathymetry uncertainty of ~ 85 m and is relatively spatially
2925 uniform. This is because each gridded gravity data point is contaminated with
2926 independent noise of varying levels during the Monte Carlo sampling. It is this
2927 point-by-point random noise that creates the noisy component in the final inverted
2928 bathymetry. In reality, the uncertainty of nearby gravity data is likely correlated,
2929 where entire lines, or sections of lines have similar uncertainty values, due to chang-
2930 ing data collection conditions, like turbulence, or mis-levelling, causing values of
2931 entire lines to be offset, or tilted. Here our ^{estimate of} gravity uncertainty is entirely depen-
2932 dent on cross-over mistakes; likely an oversimplified estimation of uncertainty for an
2933 entire survey. This suggests that the true uncertainty resulting from the gravity
2934 data likely has a different spatial distribution and may be larger than we report; a
2935 finding which should not be surprising, since the entire method depends on this data.

2936

2937 Constraints component

2938 The uncertainty in the other data input to the inversion, the constraint point depths,
2939 has only a small effect on the results (Figure 4.16b). It is worth noting that while
2940 the uncertainty resulting from the constraint point measurement uncertainty is low,
2941 the constraints themselves are fundamental to the inversion. These constraints feed
2942 into all the components of the inversion and thus affect the uncertainty of each
2943 component, including the uncertainty from the gravity data. This is shown by the
2944 correlation between uncertainty and the distance to the nearest constraint (Figure
2945 4.10) of all the components of Figure 4.16. This Monte Carlo sensitivity analysis
2946 only tests the effects of estimated noise in the inputs, and not their overall impor-
2947 tance for the inversion. Since the uncertainty in the constraints only impacts the
2948 inversion in the immediate vicinity of the constraint, for constraint data collection,
2949 efforts should be focused on quantity over quality, assuming the uncertainty can
2950 be limited to a reasonable amount. In practice, for over-ice seismic surveying, this
2951 may lead to the choice of fast and efficient systems as opposed to high-resolution
2952 systems. For example towable snow streamers and sources such as surface detona-
2953 tions or vibroseis (e.g., Hofstede et al., 2020; Smith et al., 2020b) can collect data
2954 very efficiently (~ 20 km / day), compared to higher-resolution surveys with buried
2955 geophone arrays and drill-emplaced explosives (e.g., Horgan et al., 2013). The re-
2956 maining sources of uncertainty are related to user-defined inversion parameters.

2957

2958 Density component

2959 The choice of density values for the ice, water, and sediment results in a mean un-
2960 certainty in the bathymetry model of 24 m (Figure 4.16c). The range of densities
2961 tested in the Monte Carlo simulation were $\sim 905 - 925 \text{ kg m}^{-3}$ for ice, $\sim 1015 -$
2962 1035 kg m^{-3} for seawater, and $\sim 1600 - 3000 \text{ kg m}^{-3}$ for the seafloor. We only test
2963 homogeneous changes in the density values.

2964

2965 The uncertainty arising from the choice in density values has a strong spatial cor-
2966 relation with the absolute value of the inversion's input gravity, the residual gravity
2967 (Figure 4.12d). This correlation can be explained by the inverse relation between
2968 the amplitude of the corrections applied to the bathymetry during the inversion,
2969 and the density contrasts used in the inversion. For the same gravity anomaly, a
2970 smaller density contrast results in a larger amplitude correction while a larger den-
2971 sity contrast results in a smaller correction. This means that changes in the density
2972 values just affect the amplitude of the correction applied to the bathymetry. Often,
2973 spatially variable density is used as a means to account for the regional component
2974 of gravity (e.g., Tinto et al., 2019; Constantino et al., 2020). We note that there
2975 is an additional benefit to incorporating spatially variable densities. If adequate
2976 *a priori* information is known to justify a density distribution, this can be used
2977 to allow differing amplitudes of corrections across the inversion domain. In other
2978 words, if the seafloor truly is denser in one region of the inversion compared to the
2979 seafloor elsewhere, for a similar gravity anomaly, the inversion correction should be
2980 of smaller amplitude in the high-density region. However, due to a lack of geologic
2981 knowledge beneath the ice shelf, we use constant density values. We propose Monte
2982 Carlo sampling of a wide range of possible density values as a robust and feasible
2983 method to avoid biasing the resulting bathymetry model to either too high or too
2984 low correction amplitudes, to achieve both the most realistic results and an estima-
2985 tion of the uncertainty.

2986

2987 Interpolation component

2988 The final components of the overall uncertainty are related to interpolation con-
2989 ducted during two stages of the inversion; 1) the interpolation of the starting model
2990 from the sparse constraint point depths, and 2) the estimation of the regional field
2991 from the interpolation of gravity values at the constraint points. Here, we have used
2992 a minimum curvature gridding algorithm (Smith & Wessel, 1990), which accepts a
2993 tension factor for the interpolation which can range from 0 to 1. Figure 4.9 shows
2994 the results of six different values of this tension factor for creating the starting bed
2995 model. These figures show that low values of tension are able to accurately reproduce
2996 the data with a smooth interpolation, but can result in unconstrained local maxima
2997 or minima. Conversely, high tension values produce smooth surfaces without false
2998 oscillations but don't adhere to the data as well. For these issues associated with
2999 the two end members, intermediate values of 0.25 and 0.35 are often suggested for
3000 potential field data and topographic data, respectively. We suggest a more robust
3001 alternative to using these suggested values is the Monte Carlo sampling approach
3002 we have used. This runs the inversion with a variety of tension factors and uses
3003 the standard deviation of the resulting bathymetry models as a means to estimate
3004 the uncertainty associated with the choice of the tension factor. While tensioned

3005 minimum curvature gridding has been used in several past inversions (e.g., Yang
3006 et al., 2021; Millan et al., 2020; An et al., 2019a), the choice of the tension values
3007 has not been discussed for these applications.

3008

3009 The uncertainties arising from the choice of tension factors are shown in Figure
3010 4.16d and e. The tension factor for gridding the starting bed model results in a
3011 relatively low uncertainty with a mean of 7 m. The resulting uncertainty for the
3012 regional separation is comparatively high, with a mean of 24 m. Both of these re-
3013 sults show large spatial heterogeneity, with significantly larger uncertainties along
3014 the Transantarctic Mountain front. This is likely related to the poor performance
3015 of this gridding algorithm for high-gradient data. This region along the mountain
3016 front has both steep topography and high amplitude gravity anomalies.

3017

3018 Reducing uncertainties

3019 Of the various components of the uncertainty analysis, only some can feasibly be
3020 reduced. Reducing the uncertainty resulting from the interpolation parameters may
3021 be possible with future method development, but this is beyond the discussion of this
3022 research. To our knowledge, there is no robust method of determining a spatially
3023 variable density distribution to be used in the inversion, without the collection of in-
3024 situ data. This leaves the data inputs, gravity and constraints, as viable components
3025 of a bathymetry inversion where further reductions of uncertainties can occur. We
3026 propose a favorability of quantity over quality for constraint data, since typical bed
3027 elevation uncertainty is already relatively low, and therefore more data of mediocre
3028 quality should be prioritized over high quality but spatially limited data. In order
3029 to reduce the uncertainty component resulting from the gravity data, first we must
3030 be able to estimate the realistic spatial uncertainty of the gravity data itself. A
3031 simple cross-over analysis is too simple to cover the effects of turbulence, changing
3032 flight speed and altitude, and errors in processing steps, such as base station ties
3033 and levelling. The areas of largest uncertainty are generally a function of 1) distance
3034 to the nearest constraint point (Figure 4.10) and 2) proximity to steep gradients of
3035 topography and/or gravity (Figure 4.16d and e). This highlights the entire ~~East~~
3036 ~~Antarctic Ice Sheet~~ grounding zone of the Ross Ice Shelf, and the two major con-
3037 straint gaps in the central-east portion of the ice shelf (Figure 4.10) as locations
3038 that would greatly benefit from additional seismic surveying.

3039 Past estimations of uncertainty

3040 Our comprehensive uncertainty and sensitivity analysis is shown to be similar to the
3041 approximated uncertainties reported for other ice shelves (Table 4.1). Some differ-
3042 ences include; our reported uncertainty resulting from the gravity data uncertainty
3043 is the highest reported, while our values resulting from other sources, and the total
3044 uncertainty, were similar to those of other studies. Our larger reported uncertainty
3045 resulting from the gravity data likely shows that the simple Bouguer slab approx-
3046 imation used by the other studies underestimates the component of uncertainty
3047 resulting from the gravity data uncertainty. We take the uncertainties resulting
3048 from geologic variations to be the combination of our reported uncertainties from
3049 the chosen density values (Figure 4.16c) and from the regional separation gridding
3050 (Figure 4.16e) since these both affect the estimation of the regional component. The
3051 uncertainty resulting from the constraint point measurement uncertainty was very

TAM

3052 similar across all studies.

3053
3054 From this, we propose future bathymetry inversions undertake similar uncer-
3055 tainty analysis through the Monte Carlo sampling of the input parameters. This
3056 technique not only provides similar uncertainty estimates to past studies, but it ac-
3057 complishes it in a systematic and reproducible method. Additionally, this technique
3058 provides a spatial distribution of the uncertainties, instead of a single value. Once
3059 the inversion workflow is set up, the sampling and re-running of the inversion is a
3060 simple procedure, and with the use of Latin hypercube sampling, we have shown
3061 that with only 10 runs, the parameter space of all the inputs is adequately sampled
3062 (Figure 4.8).

3063

3064 4.5.2 Past bathymetry models

3065 Our gravity-inverted bathymetry model for the sub-Ross Ice Shelf reveals significant
3066 differences with previous bathymetry models. However, a portion of these differences
3067 are not related to the inversion, but to the creation of the starting model. First,
3068 we will discuss the differences between our starting bathymetry model and another
3069 interpolation-based bathymetry model, then we will compare our inversion results
3070 with two past models. These past models include Bedmap2 (Fretwell et al., 2013)
3071 and BedMachine v3 (Morlighem et al., 2020; Morlighem, 2022). The Bedmap2
3072 model for the Ross Ice Shelf region is created from the interpolation of the same
3073 constraint points within the ice shelf as used in this study, as well as grounded ice
3074 thickness measurements and limited rock outcrop elevation data (Fretwell et al.,
3075 2013; Le Brocq et al., 2010; Timmermann et al., 2010). BedMachine v3 used these
3076 point measurements and applied additional methods to increase the resolution of
3077 the bed. For outside of the ice shelf, this included mass conservation for areas of
3078 fast-moving ice (outlet glaciers and ice streams), streamline diffusion for regions of
3079 slow-moving ice, as well as minimum curvature gridding to interpolate the remaining
3080 gaps (Morlighem et al., 2020). Within the ice shelf, BedMachine used the gravity
3081 inversion results of Tinto et al. (2019).

3082

3083 Starting model comparison

3084 Figure 4.9 shows the series of six starting bed models we created from the interpola-
3085 tion of the sparse constraints. These were created with six levels of tension applied
3086 to a minimum curvature interpolation. The cell-wise standard deviation of these
3087 six models shows the uncertainty associated with this interpolation (Figure 4.9g),
3088 and the mean of the six grids is our chosen starting model (Figure 4.9h). This is
3089 compared with the Bedmap2 model in (Figure 4.9i). The RMS difference between
3090 the two grids, within the ice shelf, is 95 m. Our starting bed is deeper around the
3091 entirety of the grounding zone, while it is shallower along the ice front and through-
3092 out the center of the ice shelf. However, these differences of up to 200 m do not
3093 suggest our starting model is inaccurate. Sampling the grid values at the constraint
3094 points and comparing them with the constraint depths shows that our model was
3095 significantly better at adhering to these constraints, compared to Bedmap2. The
3096 RMS of the difference with our model was 14 m, while the RMS of Bedmap2 was

3097 138 m (Figure 4.1).

3098

3099 These large differences for Bedmap2 are concentrated along the Transantarctic
3100 Mountain front, where the interpolation algorithm used in Bedmap2 resulted in ex-
3101 cessively shallow bathymetry. This interpolation appears to have favoured smooth-
3102 ness over accuracy for this location of steep terrain. This has resulted in a "leakage"
3103 of the high elevations within the mountains into the bathymetry interpolation, as
3104 pointed out in this region (Le Brocq et al., 2010), as well as for other ice shelves
3105 (Brisbourne et al., 2020). This over-smoothing and "leakage", while strongest along
3106 the mountain front, can be seen along the entire grounding zone. This is the reason
3107 why Bedmap2 was more shallow than our starting model along the grounding line.
3108 This shows that care needs to be taken when picking or creating a starting model for
3109 an inversion, especially in regions of steep topography. The re-creation of the start-
3110 ing model from the point data allows the choice of interpolation techniques better
3111 suited for the region of interest, compared to techniques determined most suitable
3112 for a continent-wide study.

3113

3114 Inversion result comparisons

3115 Bedmap2 comparison

3116 Figure 4.17 compares our final bathymetry results with the models of Bedmap2 and
3117 BedMachine v3. Additionally, several profiles across different regions are shown in
3118 Figure 4.18, comparing the various models. Interestingly, the inversion has raised
3119 the RMS difference with Bedmap2, compared to the starting model. But due to the
3120 issues with the Bedmap2 grid along the mountain front, this increased difference
3121 is expected. The differences between our inverted bed and Bedmap2 have a nor-
3122 mal distribution (Figure 4.17d). Our results introduce many small-scale features,
3123 as expected since Bedmap2 is an inherently smooth product. However, there are
3124 several noticeable large-scale differences with Bedmap2. Along the grounding line,
3125 our results are generally deeper, as seen with the starting model comparison (Figure
3126 4.18G). Many of the regions where our results are deeper are related to the issue of
3127 over-shallow interpolation of Bedmap2. Portions of the grounding zone along the
3128 Siple Coast are over 200 m deeper, including the Kamb (Figure 4.18c) and Mercer
3129 ice stream grounding zones.

low w/ cmt

g line
genuinely
through
f & t
ice sheet -
ice shelf
trend
perhaps
at a front
where
appropriate

3130

3131 Another notable difference is an NW-SE oriented trough which appears in our
3132 results but is essentially absent in Bedmap2. This feature begins at the southern
3133 end of the Crary Ice Rise grounding zone and continues ~ 300 km, paralleling the
3134 mountain front (Figure 4.18c). This feature is the southwestern-most of a series of
3135 2 or 3 parallel troughs and ridges, as shown in Figure 4.18d. These features are
3136 oriented at a high angle to both E-W and N-S flight lines, increasing their likelihood
3137 as true features of the bathymetry and not flight line levelling artifacts. While they
3138 are subtle, their presence alters the general *texture* in the region from a primary
3139 N-S / NNE-SSW to an NW-SW orientation. This switches the general trend of
3140 bathymetry features in the region to be aligned with Siple Coast ice flow, rather
3141 than the Transantarctic outlet glacier ice flow. Whether these bedforms are tectonic
3142 in nature, revealing the tectonic fabric, or are erosion/depositional, and thus reveal-
3143 ing the past flow directions of the previously grounded ice sheet is unknown. The

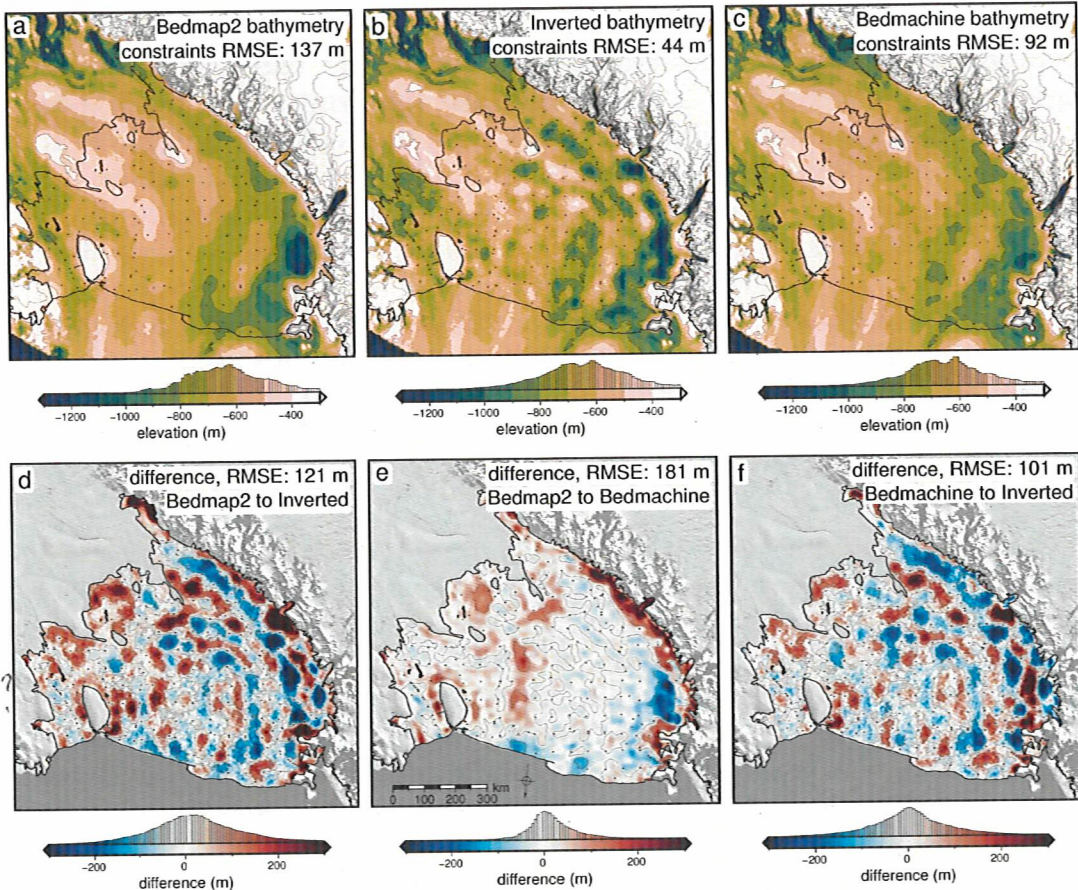


Figure 4.17: Comparison of our inverted bathymetry with past models. **a)** Bedmap2 bathymetry, **b)** our inversion results, from the weighted mean of the full Monte Carlo simulation, and **c)** bedmachine bathymetry. All three share the same colour scale and are contoured at 400 m intervals. RMS difference with the constraint points for each model is stated on the maps. **d)** Difference between our model and Bedmap2, **e)** difference between Bedmap2 and Bedmachine v3, and **f)** difference between our model and Bedmachine v3. Grids share a colour scale and are contoured at 100 m intervals. Blue regions in **d** and **f** indicate where our results are shallower, while red regions indicate where our results are deeper than the past models. Blue regions in **e** indicate where Bedmachine is shallow, while red regions indicate where Bedmachine is deeper than Bedmap2. RMS differences are stated on the maps. Grounding line and coastline are shown in black (Morlighem, 2022). Background imagery is from Scambos et al. (2007). Elevations are referenced to the WGS-84 ellipsoid.

3144 last major difference with Bedmap2 is a significantly deeper bathymetry along the
 3145 western edge of Roosevelt Island (Figure 4.18a)

3146

3147 Bedmachine comparison

3148 Comparing our results to Bedmachine v3 provides a unique opportunity to evaluate
 3149 the differences resulting from different gravity inversion algorithms. The gravity
 3150 inversion results of Tinto et al. (2019), which comprise the Bedmachine v3 data be-
 3151 neath the ice shelf, used similar input datasets (gravity data and constraint points),
 3152 suggesting that differing inversion algorithms and workflows are likely responsible
 3153 for the majority of the differences shown in Figure 4.17f. However, some of the
 3154 differences may arise from re-processing the gravity data, and a different method of
 3155 gravity reduction applied here, as compared in Section 4.3.

3156

3157 To remove the regional component of gravity, Tinto et al. (2019) used a smoothly
3158 varying density model in their inversion. To create this density model, they created
3159 an initial prism layer with prisms extending from their starting bathymetry to a
3160 depth of 60 km. With the gravity disturbance, they performed a density inver-
3161 sion to recover the density of each prism. This spatially variable density was then
3162 low-pass filtered, with a 50km cutoff. Incorporating this remaining long-wavelength
3163 gravity signal within the density model removed the regional component from the
3164 gravity input to the inversion. This technique is conceptually similar to high-pass
3165 filtering the gravity data to remove the long-wavelength component. For the in-
3166 version, Tinto et al. (2019) used the commercial software Geosoft Oasis Montaj.
3167 Limited information is available from Geosoft as to the specifics of this inversion
3168 procedure.

3169

3170 Comparing our bathymetry (Figure 4.17f), there is a normal distribution of dif-
3171 ferences, centred on zero. The RMS difference between the two grids is \sim 100 m.
3172 Comparing each grid to the constraint point depths, the BedMachine grid has an
3173 RMS difference of 92 m, compared to our RMS of 44 m. Generally, our results are
3174 approximately 50-100 m deeper along most of the Siple Coast grounding zone. Con-
3175 versely, our results are approximately 50-100 m shallower along the Transantarctic
3176 Mountain front. This could be due to our inability to fully fix the "leakage" of high-
3177 elevation data into the bathymetry depths along the mountain front in the creation
3178 of our starting model.

3179

3180 Alternatively, the differences could be a result of the different gravity reduction
3181 steps. Figure 4.12b and e show that correcting the gravity disturbance for the terrain
3182 mass effect results in a large negative topo-free disturbance along the Transantarctic
3183 mountain front (dark blues in b). During the regional field estimation, fitting
3184 a spline to these large negative values would bring down the nearby regional field,
3185 resulting in an underestimation of the regional (more negative), and thus an over-
3186 estimation of the residual (positive values). This is shown by the profile of Figure
3187 4.12e. On the right side, along the mountain front, in an attempt to fit the negative
3188 values of the topo-free disturbance (red dashed line), the regional field (blue) has
3189 been underestimated, leaving a large positive residual anomaly (pink dashed). This
3190 positive residual results in a shallowing of the inverted bathymetry.

3191

3192 These shallower depths along the mountain front, instead, could be revealing a
3193 flaw in the constraint point minimization assumption of the residual being 0 at con-
3194 straints. While the constraint point itself doesn't contribute to the residual signal,
3195 since the actual bed is equal to the starting bed at those points, deviations between
3196 the actual bed and the starting bed in the vicinity of the constraints may lead to
3197 a non-zero residual at the constraint. In this case, the interpolation of the regional
3198 field attempts to smoothly connect extremely negative values at the grounding line,
3199 and high values at the nearby constraints. This high gradient leads to poor inter-
3200 polation. This can be seen in 4.12e where the regional (blue line) is forced exactly
3201 equal to the topo-free disturbance (red dashed line) at the constraint point at 700
3202 km along the profile. In reality, the residual gravity at that constraint is likely non-
3203 zero. A non-zero value may allow the regional field to closer match the large positive
3204 topo-free disturbance located at 720 km.

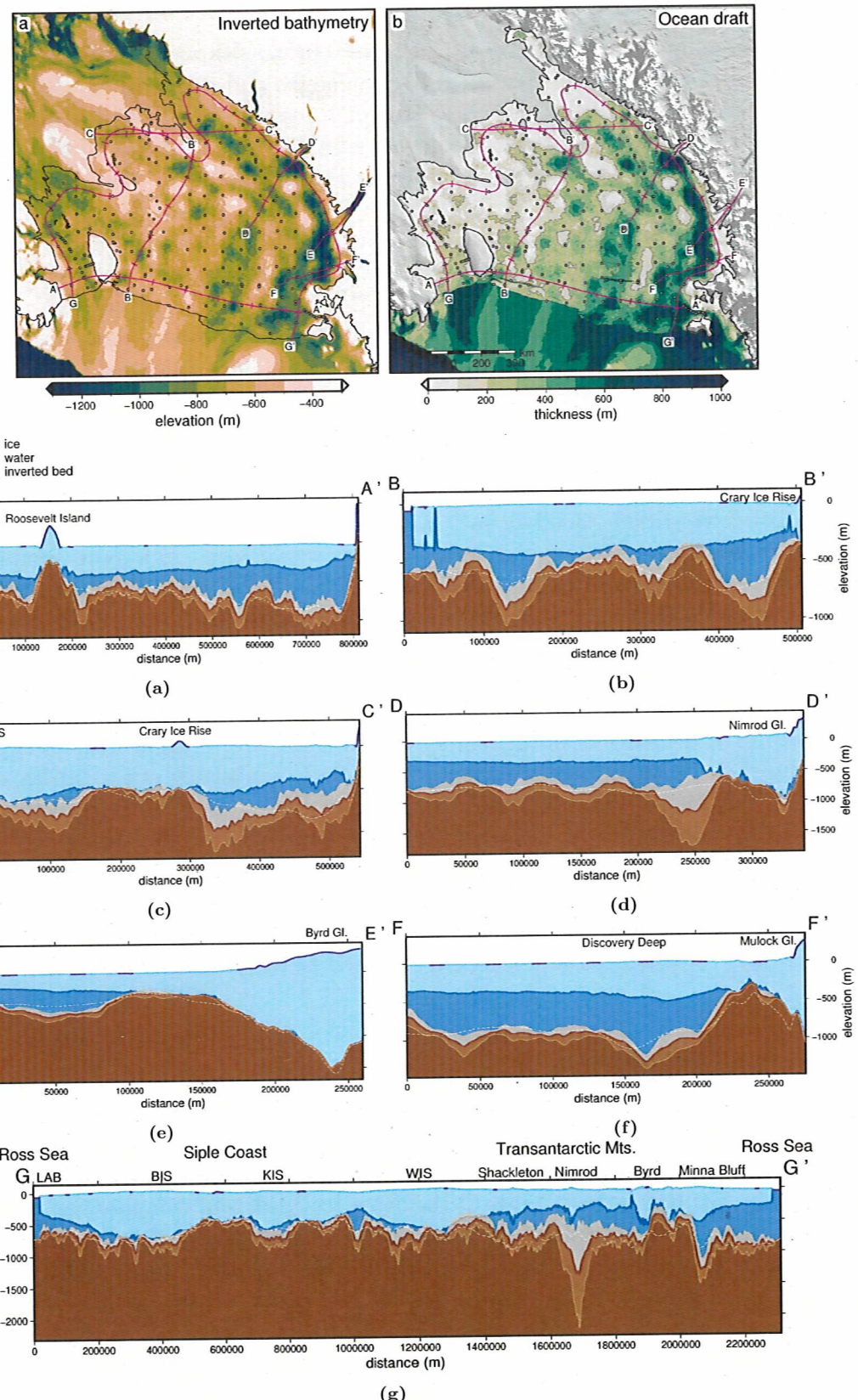


Figure 4.18: Upper panel) Ross Ice Shelf inverted bathymetry (left) and ocean draft (bed to icebase) relative to Bedmachine v3 ice base (Morlighem et al., 2020; Morlighem, 2022). Profile locations are shown in pink, with labelled endpoints and ticks every ~ 100 km. Grounding line and coastline in black (Mouginot et al., 2017). Profiles A-G) Various cross-sections showing the ice layer (light blue), water layer (darker blue), and bathymetry (brown), with uncertainties (light shade). Dotted and dashed gray lines are Bedmap2 and Bedmachine v3 bathymetry, respectively.

3205

3206 The remaining major differences between our results and BedMachine v3 in
3207 include the same series of alternating NW-SE troughs and ridges as discussed above,
3208 an ~100 m deeper region on the west side of Roosevelt Island, and a significantly
3209 deeper (~250 m) trough spanning from the south side of Minna Bluff to the outlet
3210 of the Byrd Glacier. The depths we model in this trough are $\sim 1400 \pm 150$ m. Pre-
3211 liminary results of a seismic survey at Discovery Deep, just south of Minna Bluff,
3212 in the 2021/2022 field season report depths up to 1450 m, confirming our results in
3213 this region. This seismic data was not included in this inversion. *(Similar to compare to this seismic survey in earlier section)*

3214

3215 Comparing the various difference maps of Figure 4.17 shows that our inversion
3216 has resulted in more varied topography across the ice shelf compared to Tinto et al.
3217 (2019). This increased amplitude is likely due to the differences in densities used
3218 between the inversions. Tinto et al. (2019) used a spatially variable density model,
3219 which ranged from $\sim 2600 - 2800$ kg m⁻³, with a mean of ~ 2700 kg m⁻³. While we
3220 used a spatially-constant density value, in the Monte Carlo analysis the density was
3221 varied between $\sim 1800 - 3000$ kg m⁻³, with a mean of ~ 2400 kg m⁻³. This ~ 300 kg
3222 m⁻³ difference between the mean density values would result in a more subdued in-
3223 verted bathymetry from the (Tinto et al., 2019) model. While the Tinto et al. (2019)
3224 density model does a good job of removing the regional field prior to the inversion,
3225 whether or not the density values used are representative of the seafloor is questioned
3226 here. The lowest values in their model of approximately 2600 kg m⁻³ represent the
3227 upper end of sedimentary rock densities (Schön, 2015), and are significantly greater
3228 than expected densities of unconsolidated sediments. For a region with an expected
3229 continuous drape of seafloor sediments (Chapter 2, Tankersley et al., 2022), we be-
3230 lieve the densities used in (Tinto et al., 2019) to be too high. This explanation for
3231 the differences between the inversion results is supported by the strong correlation
3232 between our bathymetry uncertainty resulting from the choice in density (Figure
3233 4.16c) and the difference between the inversion results (Figure 4.17f). This shows
3234 the importance of picking a plausible density value, and the added benefit of testing
3235 many values to estimate the uncertainty related to the chosen density value.

3236

3237 Ocean draft comparison

3238 Due to the smoothness of the base of an ice shelf, relative to bathymetry, the water
3239 column thickness beneath many ice shelves is predominately determined by the
3240 bathymetry. We use BedMachine v3 ice base elevations and our updated bathymetry
3241 to calculate the ocean draft beneath the Ross Ice Shelf and compare the results to
3242 the ocean drafts of Bedmap2 and BedMachine (Figure 4.19). These differences are
3243 very similar to those described above, due to the smooth nature of the ice base.
3244 Notable areas where our results show a thicker ocean cavity (within uncertainty
3245 ranges) compared to past models include;

- 3246 1. the Kamb grounding zone ($\sim 100 \pm 50$ m thicker, Figure 4.18c near km 100)
How about @ our seismic surveys?
- 3247 2. the west side of Crary Ice Rise ($\sim 300 \pm 150$ m thicker, Figure 4.18c near km
3248 350)
- 3249 3. the south side of Minna Bluff ($\sim 300 \pm 200$ m thicker, Figure 4.18g near km
3250 2100)

- 3251 4. the west side of Roosevelt Island ($\sim 200 \pm 100$ m thicker, Figure 4.18a near
 3252 km 220))

3253 Notable areas where our results show a thinner cavity include;

- 3254 1. the grounding zone north of Byrd Glacier ($\sim 300 \pm 50$ m thinner, Figure 4.18g
 3255 near km 2000))
- 3256 2. three 50 km wide regions in the central ice shelf, which are up to 200 ± 50 m
 3257 thinner
- 3258 3. several points approximately 50 km off of the Transantarctic Mountain front
 3259 which are up to 400 ± 50 m thinner (Figure 4.18c near km 450)

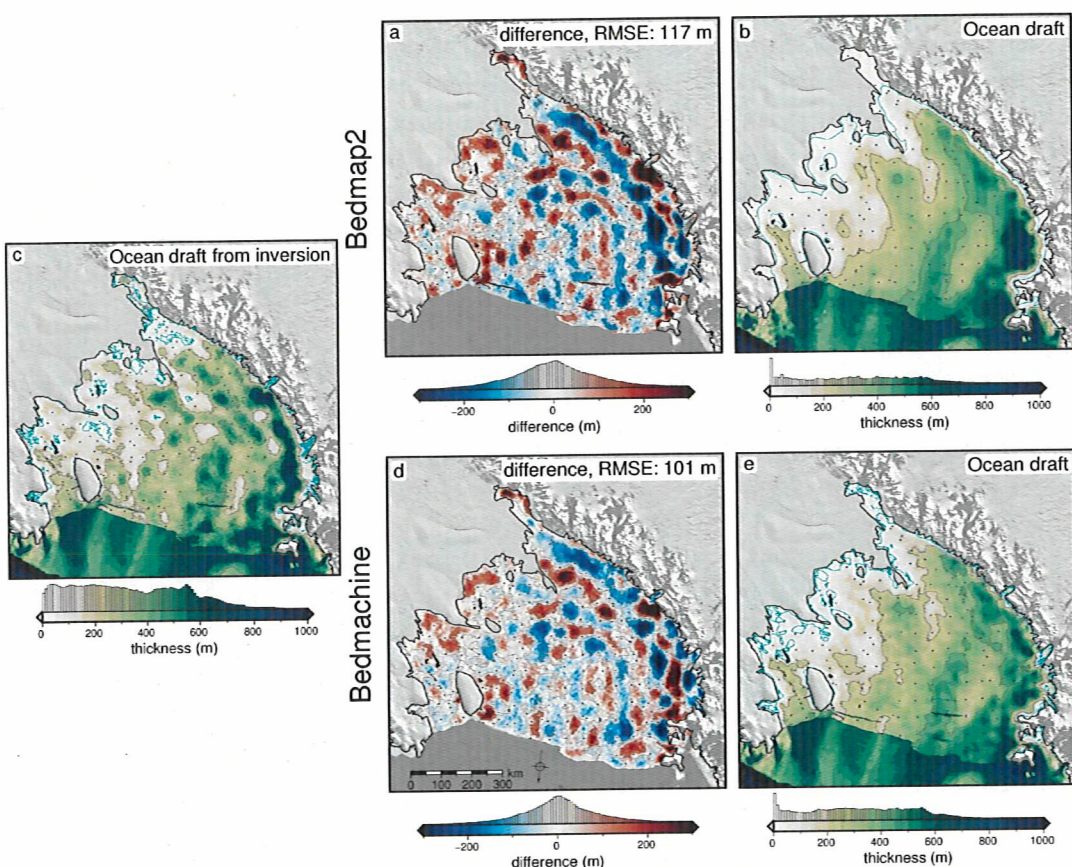


Figure 4.19: Comparison of our updated water column thickness with past models. **a)** Difference between our model and the ocean draft from Bedmap2, and **b)** the Bedmap2 ocean draft. **c)** Water column thickness calculated as the difference between BedMachine v3 icebase and our inverted bathymetry. **d)** Difference between our model and the ocean draft from BedMachine v3, and **e)** the BedMachine v3 ocean draft. Blue regions in the difference maps indicate where our results ocean draft is thinner, while red regions indicate where our results are thicker than the past models. Grounding line and coastline are shown in black (Morlighem, 2022). Background imagery is from Scambos et al. (2007). Ocean draft grids are contoured at 200 m intervals, and the 20 m contour is shown in bright blue. The difference grids are contoured at 100 m intervals. Ocean draft grids and difference grids share common colour scales.

3260 4.5.3 Implications

3261 Here, we discuss several of the important implications of our updated sub-RIS
3262 bathymetry. These implications relate to geology, tectonics, and the stability of
3263 the Ross Ice Shelf.

list in same order you present.

3264 New pinning points

3265 We have identified several areas of thin water column thickness (< 20 m) with our
3266 updated results beneath the Ross Ice Shelf. These areas are shown by the 20 m
3267 ocean draft contour, in bright blue in Figure 4.19a. These include a ~100x100 km
3268 region SW of Roosevelt Island, several ~50x50 km regions on the north flank of
3269 Crary Ice Rise (Figure 4.18g at km ~ 900), and a widespread region south of Crary
3270 Ice Rise (Figure 4.18g at km ~ 1350). Thin water depths south of Crary Ice Rise
3271 have also been modelled by a local gravity survey along the Whillans Ice Stream
3272 grounding zone (Muto et al., 2013b). Additionally, two smaller regions of sub-20 m
3273 ocean draft are found nearer the centre of the ice shelf. One is approximately 100
3274 km off the point of Crary Ice Rise and is ~ 400 km² (Figure 4.18c at km ~ 200).
3275 The second is ~ 200 km north of Crary Ice Rise and is slightly smaller (Figure 4.18b
3276 at km ~ 350). None of these shallow draft regions are present in either of the past
3277 models. Interestingly, these regions coincide with some of the lowest uncertainties
3278 we report ~ 20 m. A portion of this low uncertainty may be related to the inver-
3279 sion constraining the bathymetry to the ice base, which in regions of thin draft will
3280 reduce the variability of the suite of inversions in the Monte Carlo simulation which
3281 were used to define the uncertainty.

3282

3283 These new-identified shallow regions highlight where the Ross Ice Shelf was
3284 grounded in the recent past, or could likely become re-grounded in the future. While
3285 some of these regions are small, analysis of pinning points on the Ross Ice Shelf has
3286 shown some of the smallest pinning points can create the largest effective resistance
3287 on the ice shelf (Still et al., 2019). Additionally, some of these locations (north side
3288 of Crary Ice Rise) are predicted to have on the order of 1 m/yr of basal accretion
3289 (Adusumilli et al., 2020). An already thickening shelf within ~20 m of the bed will
3290 likely affect the ice sheet dynamics as part of future projections of the ice shelf. In-
3291 corporation of these localities of likely past pinning points may aid in resolving the
3292 ongoing debate of the style of grounding line retreat and readvance of the Ross Ice
3293 Shelf throughout the Holocene (Venturelli et al., 2020; Lowry et al., 2019; Kingslake
3294 et al., 2018).

3295

3296 4.5.3.1 Basal melting

3297 Our updated bathymetry, water column thickness, and uncertainty maps provide
3298 additional information vital to understanding the distribution of basal melt beneath
3299 the ice shelf. Melt beneath the Ross Ice Shelf is thought to predominantly occur
3300 1) along the ice front, where Antarctic Surface Water causes rapid melting in the
3301 summer (Figure 4.20 Moholdt et al., 2014; Horgan et al., 2011), and along the deep
3302 grounding zones of the Transantarctic Mountain front, where contact with High
3303 Salinity Shelf Water induces melting (Figure 4.20b Adusumilli et al., 2020; Tinto
3304 et al., 2019). Throughout the centre of the ice shelf are zones of refreezing (Figure

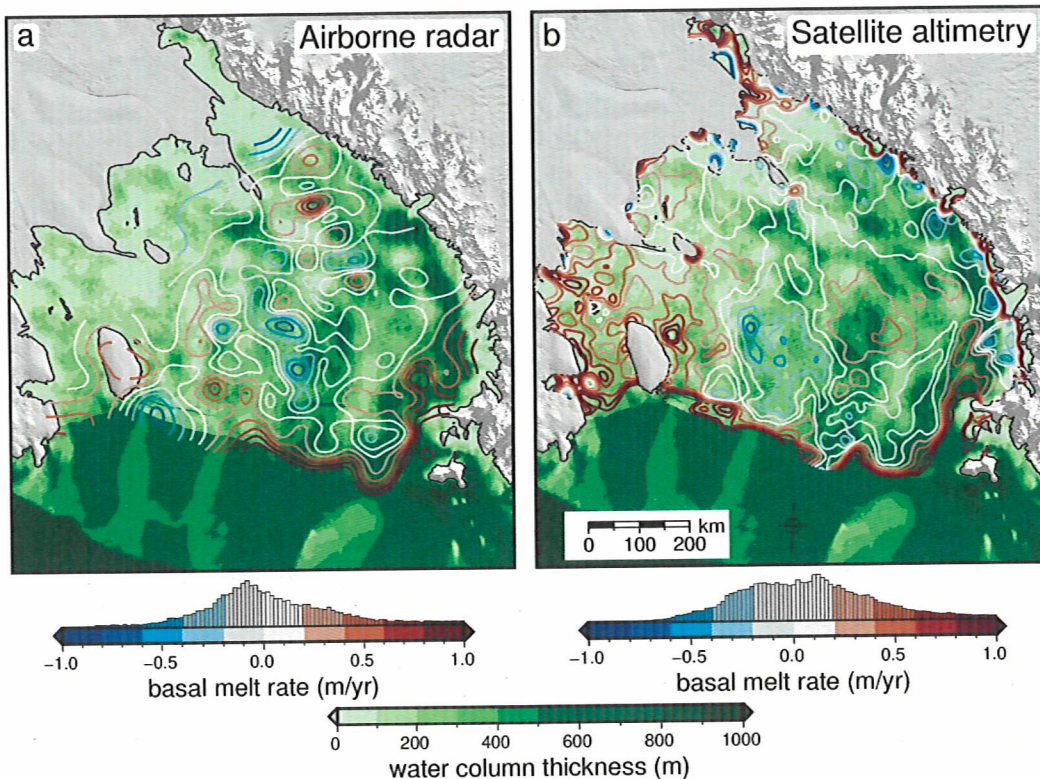


Figure 4.20: Basal melt rate and water column thickness compared for the Ross Ice Shelf. a) Blue to red contours show interpolated basal melt rate from Das et al. (2020) derived from ROSETTA-ice airborne ice-penetrating radar. Background shows ocean draft from this study. b) Same as a but with basal melt rate from Adusumilli et al. (2020) derived from satellite altimetry. Black line is the grounding line from Mouginot et al. (2017). Background imagery is from MODIS-MOA (Scambos et al., 2007).

4.20 Adusumilli et al., 2020; Das et al., 2020). Overall basal melting of the Ross Ice
 Shelf is thought to be low compared to other shelves due to the blocking of warm
 Circumpolar Deep Water from entering the cavity. This blocking is from a layer of
 dense High Salinity Shelf Water (Tinto et al., 2019; Dinniman et al., 2011). Tinto
 et al. (2019) identified the Hayes Bank (Figure 4.1b) as one location where the Cir-
 cumpolar Deep Water is able to penetrate the ice shelf cavity and induce melting,
 but this penetration is limited to the region near Roosevelt Island in their simula-
 tions. Our ocean cavity is ~ 100 m thicker than Tinto et al. (2019) immediately
 to the west of Roosevelt Island (Figures 4.18a and 4.19d). This region should be
 investigated with sub-shelf circulation models using our updated bathymetry. Our
 larger cavity allowing the inflow of warm Circumpolar Deep Water beyond Roosevelt
 Island could help explain the relatively large basal melt rate found in the region as
 shown by satellite altimetry (Figure 4.20b).

3318

3319 The high melt rates measured along the Transantarctic Mountains grounding
 zone (Adusumilli et al., 2020) are caused by the inflow of High Salinity Shelf Water
 (Tinto et al., 2019). This water is thought to be guided by bathymetric troughs and
 is able to induce melting only at large depths, due to the pressure suppression of
 the melting temperature of ice. Figures 4.20 show a comparison of both airborne
 radar and satellite altimetry derived basal melt rates to the updated ocean draft
 resulting from our bathymetry inversion. The deeper grounding zone depths both

3326 our inversion and (Tinto et al., 2019) find along the Transantarctic Mountains,
3327 compared to the depths of Bedmap2, help explain the high melt rates measured
3328 there. The other locations we report with deeper grounding zones, such as the
3329 south side of Minna Bluff, and the far southern end of the ice shelf, at the Mercer
3330 Ice Stream grounding zone, may be potential locations where High Salinity Shelf
3331 Water is able to induce basal melt. Additionally, some of the very shallow ocean
3332 drafts (< 20m) we find (Figure 4.19c), for instance to the south of Crary Ice Rise,
3333 correspond with low basal melt rates (Figure 4.20). This may be due to the lack of
3334 stratification in the water column, which occurs due to tidal mixing possible only in
3335 thin water columns (Muto et al., 2013b; Holland, 2008).

3336 **Geologic and tectonic significance**

3337 While there are many interesting implications to explore in this new dataset, we
3338 limit our discussion to several sub-Ross Ice Shelf bathymetric features of possible
3339 importance to solid-Earth investigations. These features include the bathymetry
3340 along the Transantarctic Mountain front, a deep feature on the south-west flank of
3341 Crary Ice Rise, and a newly identified orientation of bathymetry features, aligned
3342 with the Siple Coast ice streams.

3343 **Transantarctic Mountain front**

3344 The Transantarctic Mountains (Figure 4.1a) make up the world's largest rift shoul-
3345 der. Despite their prominence, the uplift mechanisms are still debated (Goodge,
3346 2020). It is likely that these mechanisms vary along-strike, and consist of some com-
3347 bination of thermal, flexural, or isostatic support (Goodge, 2020). For the central
3348 TAM, a mechanism of cantilevered flexure is proposed for the uplift of the moun-
3349 tains (Wannamaker et al., 2017; Yamasaki et al., 2008). This theoretically should
3350 be accompanied by a deep trough parallel just offshore the range front, and an
3351 outer bathymetric high, approximately 200 km from the range front (Stern & ten
3352 Brink, 1989). These features have not yet been observed (Wannamaker et al., 2017;
3353 ten Brink et al., 1993). Our results show a deep trough along the range front be-
3354 tween the Nimrod Glacier and Minna Bluff, with bathymetry highs further offshore.
3355 These features may support the theory of flexural uplift along this portion of the
3356 TAM (Wannamaker et al., 2017). Further south, where the trough disappears, the
3357 mechanism of flexural uplift is not required, since the mountains have a crustal root,
3358 which likely provides the uplift mechanism, via Airy isostasy (Wannamaker et al.,
3359 2017; Block et al., 2009).

3360 **Fault bound Crary Ice Rise**

3361 Figure 4.18c shows a profile of the updated bathymetry model across the Crary Ice
3362 Rise. Our results show a steep drop off the south flank of the ice rise (at km \sim 320),
3363 to depths up to \sim 1000 \pm 200 m. This steep drop-off is aligned with a NW-SE fault
3364 proposed by Muto et al. (2013b) from a local gravity survey along the Whillan Ice
3365 Stream grounding zone. Depth to basement analysis from magnetic data (Chapter
3366 2, Tankersley et al., 2022) also highlights this north flank of Crary Ice Rise as a
3367 likely location for faults. We believe this steep bathymetry feature adds evidence to
3368 the proposition of the Crary Ice Rise as a fault-bound horst (Muto et al., 2013b).
3369 This would imply the current grounding of the Ross Ice Shelf along the Crary Ice
3370 Rise is in part controlled by regional tectonics.

3371 New bathymetric trend

3372 From the gridding of point data, the bathymetry of the central Ross Ice Shelf is
3373 dominated by a N-S - NNE-SSW trend, aligned with the flow directions of the outlet
3374 glaciers of the Transantarctic Mountains (Figure 4.1). Our updated bathymetry
3375 model (Figure 4.15a) adds an overprinted NW-SE trend to the bathymetry features
3376 of the central portion of the ice shelf. This trend is prevalent, but subtle, in the
3377 inversion of Tinto et al. (2019). The features comprising this trend are a series of
3378 2-3 ridges and troughs of ~ 100 m amplitudes and ~ 50 km wavelengths, as shown
3379 in Figure 4.18d. These features are oblique to flight lines, adding to their validity,
3380 and are well-aligned with the Crary Ice Rise and the general ice flow direction of the
3381 Siple Coast ice streams. This trend could signify several things; 1) the most recently
3382 grounded ice in this region had a flow direction aligned with the Siple Coast ice
3383 streams, leaving behind erosional or depositional features with these orientations, 2)
3384 these features are tectonic in origin, and are the surface expressions of rift structures.
3385 These structures overprint the large bathymetric depression which runs from the
3386 Nimrod glacier to the calving front. If these are features left behind from the most
3387 recent grounding line retreat, they might inform the style of retreat. As seen in the
3388 Ross Sea, physiography of the sea floor exerts the primary control on ice stream flow
3389 and the patterns of retreat (Halberstadt et al., 2016).

3390 4.6 Conclusion

3391 Here we present an updated model of bathymetry depths beneath Antarctica's Ross
3392 Ice Shelf, as modelled from airborne gravity data. Our inversion algorithm provides
3393 a comprehensive spatial uncertainty analysis and parameter sensitivity estimation.
3394 This uncertainty highlights regions of high uncertainty that would benefit from ad-
3395 dditional seismic constraints. These regions include the entire grounding zone of the
3396 East Antarctic Ice Sheet and two points near the centre of the shelf which are up
3397 to 40 km from the nearest constraints. We summarize some key findings from the
3398 research below;

- 3399** ✓ 1. Monte Carlo sampling is a robust method of uncertainty quantification and
3400 parameter sensitivity analysis for bathymetric gravity inversions.
- 3401** ✓ 2. Sensitivity analysis shows that gravity data is the largest contributor to bathymetry
3402 uncertainty, followed by assumptions of the geology of the region.
- 3403** ✓ 3. Our updated bathymetry model better matches *a priori* sub-ice shelf measure-
3404 ments compared to past models.
- 3405** ✓ 4. Compared to Bedmap2, our results are deeper along the grounding line and
3406 shallower along the ice front.
- 3407** ✓ 5. Differences with the inversion of Tinto et al. (2019) (BedMachine v3) are
3408 mostly due to different chosen density contrasts.
- 3409** ✓ 6. Newly identified potential past pinning points are found along the Siple Coast
3410 and in the central Ross Ice Shelf.

- 3411 7. Thick ocean cavity is found along the west flank of Roosevelt Island, where
3412 ✓ Circumpolar Deep Water flows under shelf and may highlight a region of im-
3413 portance for ocean circulation modelling.
- 3414 8. Possible tectonic implications including a fault-bound Crary Ice Rise and a
3415 ✓ flexural trough associated with Transantarctic Mountain uplift.

3416 Our results provide the datasets necessary to begin answering key questions re-
3417 garding the role of the Ross Ice Shelf in various components of the Earth system.
3418 These questions include; 1) where are melt-inducing bodies of water guided beneath
3419 the ice shelf? 2) where was the ice shelf grounded in the recent past, and what was
3420 the geometry of Holocene grounding line retreat and re-advance? Are the modern
3421 bathymetry features remnants of the last grounding line retreat, or are they tec-
3422 tonic in origin? While we don't provide direct answers to these questions, without
3423 adequate knowledge of the sea floor morphology and the associated uncertainties,
3424 investigators won't have the ~~relevant~~ basic tools to answer these questions. All of the research
3425 conducted here is published as open source Python code (see Chapter 1 Section ??),
3426 with hopes that the methods presented here can be used by researchers to better
3427 model the bathymetry and uncertainty of other Antarctic ice shelves.

3465 Appendix C

3466 This appendix provides supplemental information to Chapter 4.

3467 C.1 Gravity disturbance vs anomaly

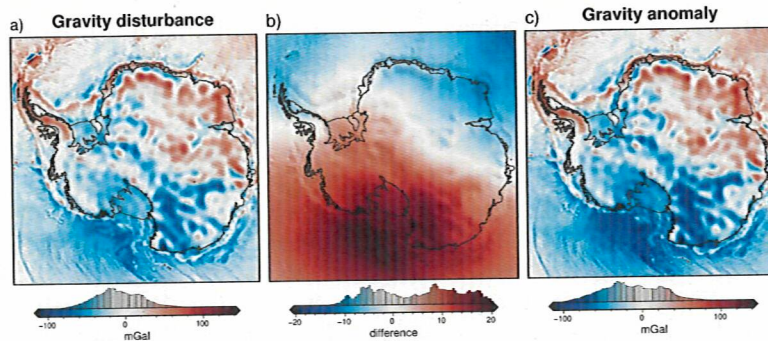


Figure C.1: Difference between the gravity disturbance and anomaly for Antarctica. Observed gravity is from Förste et al. (2014) and the normal gravity for each was calculated with the python package Boule (Project et al., 2022). See Section 4.2.1 for further details.

³⁴⁶⁸ Bibliography

- 3469 Morlighem, M., Rignot, E., Binder, T., Blankenship, D., Drews, R., Eagles, G., Eisen, O., Ferrac-
3470 cioli, F., Forsberg, R., Fretwell, P., Goel, V., Greenbaum, J. S., Gudmundsson, H., Guo,
3471 J., Helm, V., Hofstede, C., Howat, I., Humbert, A., Jokat, W., ... Young, D. A. (2020). Deep glacial troughs and stabilizing ridges unveiled beneath the margins of the Antarctic
3472 ice sheet. *Nature Geoscience*, 13(2), 132–137. <https://doi.org/10.1038/s41561-019-0510-8>
3473 (cit. on pp. 11, 17–19, 33, 62, 83, 99–101, 104–106, 108, 109, 115, 119)
3474 BedMachine
3475
- 3476 Morlighem, M. (2022). MEaSUREs BedMachine Antarctica, Version 3. (Cit. on pp. 11, 17–20, 33,
3477 83, 99–101, 104–106, 108–110, 115, 117, 119, 121).
- 3478 Adusumilli, S., Fricker, H. A., Medley, B., Padman, L., & Siegfried, M. R. (2020). Interannual
3479 variations in meltwater input to the Southern Ocean from Antarctic ice shelves. *Nature
3480 Geoscience*, 13(9), 616–620. <https://doi.org/10.1038/s41561-020-0616-z> (cit. on pp. 11,
3481 20, 33, 82, 122, 123)
- 3482 McCubbine, J. (2016). *Airborne Gravity Across New Zealand - For An Improved Vertical Datum*
3483 (Doctoral dissertation). Victoria University of Wellington. (Cit. on pp. 11, 40, 41).
- 3484 Uieda, L., & Barbosa, V. C. (2017). Fast nonlinear gravity inversion in spherical coordinates with
3485 application to the South American Moho. *Geophysical Journal International*, 208(1), 162–
3486 176. <https://doi.org/10.1093/gji/ggw390> (cit. on pp. 11, 36, 42, 43, 46, 48, 78, 91, 97)
- 3487 Dorschel, B., Hehemann, L., Viquerat, S., Warnke, F., Dreutter, S., Tenberge, Y. S., Accettella, D.,
3488 An, L., Barrios, F., Bazhenova, E., Black, J., Bohoyo, F., Davey, C., De Santis, L., Dotti,
3489 C. E., Fremand, A. C., Fretwell, P. T., Gales, J. A., Gao, J., ... Arndt, J. E. (2022). The
3490 International Bathymetric Chart of the Southern Ocean Version 2. *Scientific Data*, 9(1),
3491 275. <https://doi.org/10.1038/s41597-022-01366-7> (cit. on pp. 13, 14, 60, 61, 63)
3492 IBCSO
- 3493 Brancolini, G., Busetti, M., Marchetti, A., Santis, L. D., Zanollo, C., Cooper, A. K., Cochrane,
3494 G. R., Zayatz, I., Belyaev, V., Knyazev, M., Vinnikovskaya, O., Davey, F. J., & Hinze, K.
3495 (1995). Descriptive text for the seismic stratigraphic atlas of the Ross Sea, Antarctica. In
3496 A. K. Cooper, P. F. Barker, & G. Brancolini (Eds.), *Geology and Seismic Stratigraphy of
3497 the Antarctic Margin* (A271–A286). American Geophysical Union. <https://doi.org/10.1002/9781118669013.app1>. (Cit. on pp. 13, 60, 61)
- 3498 Mouginot, J., Scheuchl, B., & Rignot, E. (2017). MEaSUREs Antarctic Boundaries for IPY 2007–
3499 2009 from Satellite Radar, Version 2. (Cit. on pp. 16, 17, 19, 20, 82, 100–102, 119, 123).
- 3500 Scambos, T., Haran, T., Fahnestock, M., Painter, T., & Bohlander, J. (2007). MODIS-based Mosaic
3501 of Antarctica (MOA) data sets: Continent-wide surface morphology and snow grain size.
3502 *Remote Sensing of Environment*, 111(2–3), 242–257. <https://doi.org/10.1016/j.rse.2006.12.020> (cit. on pp. 16, 18–20, 82, 105, 109, 110, 117, 121, 123)
- 3503 Förste, C., Bruinsma, S., Abrikosov, O., Lemoine, J.-M., Marty, J. C., Flechtner, F., Balmino, G.,
3504 Barthelmes, F., & Biancale, R. (2014). EIGEN-6C4 The latest combined global gravity
3505 field model including GOCE data up to degree and order 2190 of GFZ Potsdam and GRGS
3506 Toulouse. <https://doi.org/10.5880/ICGEM.2015.1>. (Cit. on pp. 16, 21, 87, 135)
- 3507 Li, X., & Götz, H.-J. (2001). Ellipsoid, geoid, gravity, geodesy, and geophysics. *Geophysics*, 66(6),
3508 1660–1668. <https://doi.org/10.1190/1.1487109> (cit. on pp. 16, 85, 87)
- 3509 Fretwell, P., Pritchard, H. D., Vaughan, D. G., Bamber, J. L., Barrand, N. E., Bell, R. E., Bianchi,
3510 C., Bingham, R. G., Blankenship, D. D., Casassa, G., Catania, G., Callens, D., Conway,
3511 H., Cook, A. J., Corr, H. F. J., Damaske, D., Damm, V., Ferraccioli, F., Forsberg, R.,
3512 ... Zirizzotti, A. (2013). Bedmap2: Improved ice bed, surface and thickness datasets for
3513 Antarctica. *The Cryosphere*, 7(1), 375–393. <https://doi.org/10.5194/tc-7-375-2013> (cit.
3514 on pp. 17, 82, 83, 89, 90, 99, 115)
- 3515
- 3516

- 3517 Koch, P., Wujek, B., Golovidov, O., & Gardner, S. (2017). Automated Hyperparameter Tuning for
 3518 Effective Machine Learning. *SAS Institute Inc.* (cit. on pp. 17, 94).
- 3519 Das, I., Padman, L., Bell, R. E., Fricker, H. A., Tinto, K. J., Hulbe, C. L., Siddoway, C. S.,
 3520 Dhakal, T., Frearson, N. P., Mosbeux, C., Cordero, S. I., & Siegfried, M. R. (2020). Multi-
 3521 decadal basal melt rates and structure of the Ross Ice Shelf, Antarctica using airborne ice
 3522 penetrating radar. *Journal of Geophysical Research: Earth Surface*, 1–20. <https://doi.org/10.1029/2019JF005241> (cit. on pp. 20, 32, 123)
- 3523 Project, F. a. T., Dinneen, C., Gomez, M., Li, L., Pesce, A., Soler, S. R., & Uieda, L. (2022). Boule
 3524 v0.4.1: Reference ellipsoids for geodesy and geophysics. <https://doi.org/10.5281/zenodo.7258175>. (Cit. on pp. 21, 135)
- 3525 Tankersley, M., Horgan, H. J., Siddoway, C. S., Caratori Tontini, F., & Tinto, K. J. (2022). Base-
 3526 ment Topography and Sediment Thickness Beneath Antarctica's Ross Ice Shelf. *Geophys-
 3527 ical Research Letters*, 49(10). <https://doi.org/10.1029/2021GL097371> (cit. on pp. 27, 107,
 3528 120, 124)
- 3529 Crary, A. (1959). Oversnow Traverses from IGY Little American Station. *Transactions, American
 3530 Geophysical Union*, 40(3), 311–315. <https://doi.org/10.1029/TR040i003p00269> (cit. on
 3531 pp. 28, 83, 99)
- 3532 Bentley, C. R., Crary, A. P., Ostenso, N. A., & Thiel, E. C. (1960). Structure of West Antarctica.
 3533 *Science*, 131(3394), 131–136. <https://doi.org/10.1126/science.131.3394.131> (cit. on p. 28)
- 3534 Houtz, R., & Davey, F. J. (1973). Seismic profiler and sonobuoy measurements in Ross Sea, Antarc-
 3535 tica. *Journal of Geophysical Research*, 78(17), 3448–3468. <https://doi.org/10.1029/JB078i017p03448> (cit. on p. 28)
- 3536 Smith, B., Fricker, H. A., Gardner, A. S., Medley, B., Nilsson, J., Paolo, F. S., Holschuh, N.,
 3537 Adusumilli, S., Brunt, K., Csatho, B., Harbeck, K., Markus, T., Neumann, T., Siegfried,
 3538 M. R., & Zwally, H. J. (2020a). Pervasive ice sheet mass loss reflects competing ocean and
 3539 atmosphere processes. *Science*, eaaz5845. <https://doi.org/10.1126/science.aaz5845> (cit. on
 3540 p. 32)
- 3541 Rignot, E., Mouginot, J., Scheuchl, B., van den Broeke, M., van Wessem, M. J., & Morlighem, M.
 3542 (2019). Four decades of Antarctic Ice Sheet mass balance from 1979–2017. *Proceedings of
 3543 the National Academy of Sciences*, 116(4), 1095–1103. <https://doi.org/10.1073/pnas.1812883116> (cit. on p. 32)
- 3544 Dupont, T. K., & Alley, R. B. (2005). Assessment of the importance of ice-shelf buttressing to
 3545 ice-sheet flow. *Geophysical Research Letters*, 32, 1–4. <https://doi.org/10.1029/2004GL022024> (cit. on pp. 32, 81, 82)
- 3546 Goldberg, D. N. (2017). Ice Shelf Buttressing. In D. Richardson, N. Castree, M. F. Goodchild,
 3547 A. Kobayashi, W. Liu, & R. A. Marston (Eds.), *International Encyclopedia of Geography:
 3548 People, the Earth, Environment and Technology* (pp. 1–9). John Wiley & Sons, Ltd. <https://doi.org/10.1002/9781118786352.wbieg0567>. (Cit. on p. 32)
- 3549 Jenkins, A., Dutrieux, P., Jacobs, S. S., McPhail, S. D., Perrett, J. R., Webb, A. T., & White, D.
 3550 (2010). Observations beneath Pine Island Glacier in West Antarctica and implications for
 3551 its retreat. *Nature Geoscience*, 3(7), 468–472. <https://doi.org/10.1038/ngeo890> (cit. on
 3552 p. 32)
- 3553 Tinto, K. J., Padman, L., Siddoway, C. S., Springer, S. R., Fricker, H. A., Das, I., Caratori Tontini,
 3554 F., Porter, D. F., Frearson, N. P., Howard, S. L., Siegfried, M. R., Mosbeux, C., Becker,
 3555 M. K., Bertinato, C., Boghosian, A., Brady, N., Burton, B. L., Chu, W., Cordero, S. I.,
 3556 ... Bell, R. E. (2019). Ross Ice Shelf response to climate driven by the tectonic imprint on
 3557 seafloor bathymetry. *Nature Geoscience*, 12(6), 441–449. <https://doi.org/10.1038/s41561-019-0370-2> (cit. on pp. 32, 40, 62, 82, 83, 96–99, 102, 111, 113, 115, 117, 118, 120, 122–125)
- 3558 Pritchard, H. D., Ligtenberg, S. R. M., Fricker, H. A., Vaughan, D. G., van den Broeke, M. R., &
 3559 Padman, L. (2012). Antarctic ice-sheet loss driven by basal melting of ice shelves. *Nature*,
 3560 484(7395), 502–505. <https://doi.org/10.1038/nature10968> (cit. on pp. 32, 82)
- 3561 St-Laurent, P., Klinck, J. M., & Dinniman, M. S. (2013). On the Role of Coastal Troughs in the
 3562 Circulation of Warm Circumpolar Deep Water on Antarctic Shelves. *Journal of Physical
 3563 Oceanography*, 43(1), 51–64. <https://doi.org/10.1175/JPO-D-11-0237.1> (cit. on p. 32)
- 3564 Yang, J., Guo, J., Greenbaum, J. S., Cui, X., Tu, L., Li, L., Jong, L. M., Tang, X., Li, B., Blanken-
 3565 ship, D. D., Roberts, J. L., Ommen, T., & Sun, B. (2021). Bathymetry Beneath the Amery
 3566 Ice Shelf, East Antarctica, Revealed by Airborne Gravity. *Geophysical Research Letters*,
 3567 48(24). <https://doi.org/10.1029/2021GL096215> (cit. on pp. 32, 40, 56, 95, 97, 98, 111,
 3568 114)
- 3569
- 3570
- 3571
- 3572
- 3573
- 3574
- 3575